DISCLAIMER

This report was prepared as an account of work sponsored by an agency of the United States Government. Neither the United States Government nor any agency thereof, nor any of their employees, makes any warranty, express or implied, or assumes any legal liability or responsibility for the accuracy, completeness, or usefulness of any information, apparatus, product, or process disclosed, or represents that its use would not infringe privately owned rights. Reference herein to any specific commercial product, process, or service by trade name, trademark, manufacturer, or otherwise does not necessarily constitute or imply its endorsement, recommendation, or favoring by the United States Government or any agency thereof. The views and opinions of authors expressed herein do not necessarily state or reflect those of the United States Government or any agency thereof. Reference herein to any social initiative (including but not limited to Diversity, Equity, and Inclusion (DEI); Community Benefits Plans (CBP); Justice 40; etc.) is made by the Author independent of any current requirement by the United States Government and does not constitute or imply endorsement, recommendation, or support by the United States Government or any agency thereof.

LA-UR-25-25127

Title: Plutonium Oxidation State Distribution in the Presence of WIPP-Relevant Organics and Iron Corrosion Products

Author(s): Kaplan, Ugras

Intended for: Report

Issued: 2025-05-30

NOTICE: The current controlled version of this document is on the LCODocs website (http://lcodocs.lanl.gov/). A printed copy of the document may not be the current version.

LOS ALAMOS NATIONAL LABORATORY
CARLSBAD OPERATIONS

LCO-ACP-38, Revision 1

Plutonium Oxidation State Distribution in the Presence of WIPP-Relevant Organics and Iron Corrosion Products

Effective Date: 05/28/2025

Originator:

Ugras Kaplan Digitally signed by Ugras Kaplan Date: 2025.05.23 13:41:39 -06'00'

Ugras Kaplan, LANL-CO ACRSP Date

Approved by:

DOUGLAS WEAVER (Affiliate) Digitally signed by DOUGLAS WEAVER (Affiliate) Date: 2025.05.27 16:35:26 -06'00'

Jonathan Icenhower, LANL-CO ACRSP Team Leader Date

PRISCILLA YANEZ (Affiliate) Digitally signed by PRISCILLA YANEZ (Affiliate) Date: 2025.05.27 16:28:00 -06'00'

Priscilla Yanez, LANL-CO Quality Assurance Manager Date

DOUGLAS WEAVER (Affiliate) Digitally signed by DOUGLAS WEAVER (Affiliate) Date: 2025.05.27 16:35:49 -06'00'

Douglas Weaver, LANL-CO Division Leader Date

History of Revisions

Revision Number	Effective Date	Pages Affected	Description of Revision
0	12/18/24	All	Original Release
1	05/28/2025	1, 2, 5, 8, 10-12, 15-20, 26, 30, 37	Errors were found in the reference to the governing test plan, the documented time frame of experiments, an EXAFS spectrum, and the name in a citation. These were corrected. Other editorial changes were incorporated.

TABLE OF CONTENTS

LIST OF TABLES

LIST OF FIGURES

EXECUTIVE SUMMARY

The oxidation state and solubility of plutonium (Pu) in high ionic strength synthetic WIPP (Waste Isolation Pilot Plant) brines as a function of pC_{H+} in the presence and absence of WIPP-relevant organic ligands (EDTA [Ethylenediaminetetraacetic acid], oxalate, citrate, acetate) and iron corrosion products (magnetite and metallic iron) at $T = 23 \pm 2$ ∘C was thoroughly studied by long-term batch solubility experiments (between approximately 800-1,100 days) from an undersaturation approach.

The oxidation state of Pu in the WIPP environment has been a topic of interest since the initial Compliance Certification Application (CCA). This study aims to investigate the solubility of Pu under the expected WIPP conditions and to determine the oxidation state of the solid phase that will control the solubility.

One of the most important results of this study is that the Pu oxidation state was analyzed both from the surface area of the corrosion products and in the precipitated solid. The analysis of the Pu oxidation state on the surface of the iron mineral from the ongoing undersaturated experiments is more relevant to the performance assessment of nuclear waste disposal than short term batch (plutonium-iron phase) experiments. The X-ray Absorption Near-Edge Spectroscopy (XANES) analysis showed that Pu oxidation state is different on the metal surface and in the precipitated solid. Pu(III) is the dominant oxidation state in the metallic iron (Fe^0) system in the presence and absence of organics. Pu(IV) is the dominant oxidation state in the magnetite system in the presence and absence of organics. Also, organics stabilize Pu(IV) in the magnetite system. Analysis of Pu in the precipitated solid by Extended X-ray Absorption Fine Structure (EXAFS) analysis showed that Pu formed an inner-sphere complex with iron with minor amounts of PuO_2 present. X-ray diffraction (XRD) results indicate that metallic iron and magnetite did not oxidize in three years in the alkaline and high ionic strength system.

Under these conditions ($8 < pC_{H+} < 10$ at $T = (22 \pm 2)$ °C under nitrogen atmosphere, the solubility of Pu changes by up to three orders of magnitude (10^{-5} and 10^{-8} M). The spread in solubility is highest at $pC_{H+} = 9$. Pu(III) and Pu(IV) showed different solubility behavior in the synthetic WIPP brine.

A summary of the data collected in this report will be submitted to Sandia National Laboratories as part of a parameter update report which will outline the changes to the OXSTAT parameter for the 2026 Compliance Recertification Application (CRA-2026).

The experiments performed were done according to the U.S. Department of Energy (DOE) approved Test Plan entitled “Effects of Radiolysis, Organic Complexation, and Redox Conditions on the Speciation and Oxidation State Distribution of Pu(III/IV)” (LCO-ACP-25). All data reported were obtained under the Los Alamos National Laboratory-Carlsbad Office (LANL-CO)

Quality Assurance Program, which is compliant with the DOE Carlsbad Field Office, Quality Assurance Program Document (CBFO/QAPD).

ACRONYMS AND ABBREVIATIONS

Å	Angstrom
AgCl	Silver(I) chloride
am	Amorphous
atm	Atmospheres
°C	Degrees Celsius
C	Carbon
Ca^{2+}	Calcium in the +2 oxidation state
CBFO	Carlsbad Field Office
CCA	Compliance Certification Application
Ci	Curie
Cm(III)	Curium in the +3 oxidation state, also written Cm^{3+}
CN	Coordination Number
CRA	Compliance Recertification Application
DBR	Direct Brine Release
DOE	(United States) Department of Energy
EDTA	Ethylenediaminetetraacetic acid
E_h	Oxidation-reduction potential (vs. Standard Hydrogen Electrode)
ERDA-6	Energy Research and Development Administration Well 6
eV	Electron volt
EXAFS	Extended X-ray Absorption Fine Structure
Fe^0	Iron metal-oxidation state is 0
Fe^{2+}	Iron in the +2-oxidation state
Fe^{3+}	Iron in the +3-oxidation state
Fe_3O_4	Magnetite
FeS_2	Pyrite
GWB	Generic Weep Brine

ACRONYMS AND ABBREVIATIONS (cont.)

HPW	high purity water
I	Ionic strength of a solution
ICP-MS	Inductively Coupled Plasma Mass Spectrometry
K	Kelvin
kDa	Kilodalton
keV	Kilo electron volt
kV	Kilo volt
L	Liter
LANL	Los Alamos National Laboratory
LCF	Linear Combination Fitting
log K_{sp}	Logarithm of Solubility Product Constant
M	Molarity, moles of solute per liter of solvent
mA	Milliampere
Mg^{2+}	Magnesium in the +2-oxidation state
mag	Magnitude
min	Minute
mL	Milliliter
mV	Millivolt
nm	Nanometer
NNSA	National Nuclear Security Administration
O_{ax}	Axial Oxygen
PA	Performance Assessment
pC_{H+}	Negative log of the hydrogen ion concentration
pe	The activity of electrons in factors of 10
pH	negative log of the hydrogen ion activity
ppb	parts per billion

ACRONYMS AND ABBREVIATIONS (cont.)

ppm	parts per million
Pu(III)	Plutonium in the +3 oxidation state, also written Pu^{3+}
Pu(IV)	Plutonium in the +4 oxidation state, also written Pu^{4+}
Pu(V)	Plutonium in the +5 oxidation state, also written PuO_2^{+}
Pu(VI)	Plutonium in the +6 oxidation state, also written PuO_2^{2+}
PuO_2	Plutonium(IV) oxide
QAPD	Quality Assurance Program Document
R	Interatomic distance in Angstrom
Si	Silicon
SSRL	Stanford Synchrotron Radiation Light Source
t	Time
TC10a	ThermoChimie version 10
TRU	Transuranic
UV/Vis	Ultraviolet-visible spectrophotometer
WIPP	Waste Isolation Pilot Plant
WL	White line (refers to an intense absorption in the near edge)
XANES	X-ray Absorption Near-Edge Spectroscopy
XAS	X-ray Absorption Spectroscopy
XRD	X-ray Diffraction
Zr	Zirconium
$\sigma^2/[\text{Å}^2]$	Debye Waller factor
ΔE	Energy difference
$S_0^2(k)$	Amplitude reduction factor

1.0 INTRODUCTION

The long-term safe disposal of radioactive waste is a challenging but necessary task for our environment. Countries that have nuclear waste are looking for solutions to dispose of their waste within the framework of their natural resources. Argillaceous rock formations are under consideration as potential host rock for nuclear waste repositories in several countries (Germany, Switzerland, France, and Belgium) [Hoth et al. 2007; Kosakowski and Scherrer 2004; OECD 2006; Honty and Craen 2009]. Korea Atomic Energy Research Institute has been investigating granite systems as the host rock for high level nuclear waste [Cho et al. 2008]. The United States of America (USA) and Germany are among the leading countries in the world in terms of salt repository research, design and operation for nuclear waste [CRA 2009; Kaul and Roethemeyer 1997].

The Waste Isolation Pilot Plant (WIPP) is the nation's only deep geologic radioactive waste repository, and the first salt-based deep geologic defense related transuranic (TRU) radioactive waste repository to operate in the world. Located in Carlsbad, New Mexico, WIPP has been in operation since 1980. Recent estimates suggest that approximately 3.07×10^6 Ci (10.9 tons) of plutonium (Pu) are listed in the WIPP inventory through 2021 [Gerle 2022]; however, 34 tons of surplus Pu are being actively petitioned for disposal by the National Nuclear Security Administration (NNSA) through their dilute and dispose strategy [DOE 2023]. Pu is an important element in nuclear waste management due to its long half-life and high radiotoxicity. Understanding the speciation, oxidation state distribution, sorption-desorption processes, and solubility behavior of radionuclides is fundamental to the long-term safety assessment of repositories for nuclear waste disposal. This has been extensively reviewed for Pu [Geckeis et al. 2016; Neu et al. 2011]. The speciation, solubility behavior, and electronic states of Pu depends on local chemical conditions such as pH, E_h, complexing ligands, and ionic strength. In aqueous media, the four oxidation states of Pu(III)/(IV)/(V)/(VI) are thermodynamically stable. Under conditions relevant to subsurface, reducing waste repositories, Pu(III) and Pu(IV) species predominate [Neck et al. 2007; Clark 2000; Lemire 2001]. In contrast, some repository are designed with oxidizing conditions (e.g., Yucca) where Pu(V)/(VI) can persist.

This study focuses on the effects of organic matter and iron corrosion products present in the WIPP waste repository on the oxidation states of Pu. The most relevant research available in the literature on this system is discussed below.

Organic ligands affect the speciation of actinides, which may form oxidation state specific complexes that can increase the solubility of the metal cation and stabilize its subsequent reduction or oxidation [Runde 2000]. The WIPP-relevant organics; EDTA, oxalate, citrate, and acetate are used as a part of the nuclear industry in separation and decontamination processes and are disposed of with other wastes at WIPP [McFadden 1980; Serne et al. 2002; Delegard 1984]. These organics play a role in the speciation and oxidation state of Pu. EDTA (a polyprotic acid containing four carboxylic acid groups and two amine groups) and citrate (four functional groups, three carboxylates and one hydroxyl, of which no more than three can be bonded to a metal simultaneously due to steric constraints), are both known as strong chelators to Pu in most oxidation states.

Although the effect of organic complexation on the Pu oxidation state has been investigated since the late 1950s [Thakur et al. 2009; Almahamid et al. 1996; DiBlasi et al. 2021; DiBlasi et al. 2022; Comins et al. 2024], difficulties occur in directly adapting and comparing these results to the WIPP system. A prime difficulty is the presence of divalent cations in the WIPP system. It is known that WIPP-relevant organics are prone to complex with divalent cations such as Ca^{2+}, Mg^{2+}, or Fe^{2+} [Serne et al. 2002; Delegard 1984]. In this case, the probability of Pu forming ternary/quaternary complexes under repository conditions (high ionic strength, high alkalinity, and hydroxide formation) is very high. This causes some difficulties in the correct interpretation of the experimental data. Another difficulty is how to address the effects of chemical, microbial, and radiolytic degradation, not previously considered in experiments examining or interpreting Pu-organic interactions [Toste 1992; Toste and Lechner-Fish 1993; Francis et al. 2006].

Comins et al. (2024) performed complexation studies in Pu(VI)-citrate and Pu(III)-citrate systems (pH = 2.5-11.0, I =0.1 M NaCl under anoxic conditions). Pu(VI) species were found to be less stable in the presence of citrate (t = 168 days); the rate of reduction increased with increasing pH, and the observed Pu(III) stability increased in the presence of citrate (t = 293 days). Higher concentrations of Pu(III) were favored at lower pH. The highlight of this study provided evidence of a radiolysis-driven mechanism for the citrate-mediated reduction of Pu that involves electron transfer from the oxidative breakdown of citrate [Comins et al. 2024]. Rai et al. (2001) and DiBlasi et al. (2021, 2022) show that hydroxy-EDTA complexes are dominant at high alkalinity due to the strong affinity of hydroxide with Pu, allowing ternary-EDTA species of Pu(III) and Pu(IV) to form. The formation of ternary/quaternary Pu-metal-hydroxy-EDTA complexes is logical when accounting for the strong complexation of alkali metals with EDTA, strong hydroxide affinity for Pu, and the polydentate nature of EDTA. Recent investigations by DiBlasi et al. (2022), using curium (Cm) as a trivalent analog to Pu, revealed the formation of previously unreported An(III)–OH–EDTA, Ca–An(III)–EDTA, and Ca–An(III)–OH–EDTA complexes (An = Pu, Cm). Formation of Cm(III)–OH–EDTA complexes is dependent on pH and has been shown to incorporate Ca to form Ca–Cm(III)–EDTA at pH > 11, and an additional quaternary Ca–Cm(III)–OH–EDTA complex forms under hyperalkaline conditions (pH > 12). The presence of calcium may prevent the short-term partial oxidation of Pu(III) to Pu(IV) through the stabilization of Ca–Pu(III)–EDTA species in solution [Rai et al. 2001; DiBlasi 2021; DiBlasi 2022].

Rai et al. (2008) experimentally evaluated the solubility of $^{239}PuO_2(am)$ in the presence of ferrihydrite and EDTA in dilute solutions (pH 2.3 to 11.5). The total Pu concentrations measured in these experiments were much higher than predicted. This discrepancy was attributed to the complexation of Pu(IV) and Fe(III) by EDTA. Oxidation state analysis by solvent extraction showed significant amounts of Pu(III) were in solution below about pH 8; while Pu(V) and Pu(VI) were in solution above about pH 8. Reduction of Pu(IV) to Pu(III) in the absence of an added reductant was attributed to reactions with small amounts of ferrous iron (Fe^{2+}) in the ferrihydrite. Rai et al. (2008) concluded from their experimental data and calculations that the importance of Pu(IV)-EDTA complexes had been overstated and that Pu(III)-EDTA complexes may also play an important role in Pu mobility in reducing environments [Rai et al. 2008].

It is very important to understand the mechanisms of iron corrosion and to predict the formation of these corrosion products with high confidence. Depending on the types of corrosion products formed, the oxidation states of redox sensitive radionuclides such as Pu can be determined more reliably and accurately. Research on corrosion under anoxic saline conditions has been carried out mostly in countries that use salt rock geology for nuclear waste disposal (Germany and parts of the USA). Waste containers are the most important source of iron in nuclear waste repositories. Corrosion of steel (or metal in general) drums create a reducing environment which affects the solubility and binding constants of some actinides by reducing their oxidation states.

When examining the formation of corrosion products, the conditions in the nuclear waste repository must be evaluated correctly. Before anoxic conditions are formed in the waste storage environment, the waste storage will be oxic for a significant period. During this initial phase, the amount of oxygen will decrease over time until the second period of anoxic phases is established in the repository environment. It is important to examine these two conditions separately to properly determine corrosion product formation. Therefore, at the end of the oxic phase, the surface of the containers will be covered with a corrosion product layer rich in various amounts of Fe(III). For example, engineers have compiled data from steel bridges and other iron-based structures in marine environments and have identified magnetite as a component of the phase assemblage during corrosion [Asami and Kikucki 2003; Cook 2005]. As the redox conditions inside the repository become anoxic, the Fe(III) phases in the corrosion product film will become thermodynamically unstable and will be reduced predominantly to Fe(II) species. There is some evidence that the presence of magnetite (Fe_3O_4) corrosion products may increase the corrosion rate of carbon steel during the transition from aerobic to anoxic conditions, the most important reason being the thermodynamic stability of magnetite [Schramke et al. 2020].

Studies by Wang et al. (2000) investigated the corrosion products of carbon steel in WIPP brine (at 25 °C and pH 9.5). In this study, the formation of heterogenous phases, magnetite and green rust films carrying SO_4^{2-} and Cl^- species, was found [Wang et al. 2000]. Green rusts are metastable with respect to magnetite under anoxic conditions in the pH range of 7-9 [Tosca et al. 2018].

In the study conducted by Nemer et al. (2011), carbon steel was exposed to Na–Cl and Na–Mg–Cl-dominated brines under anoxic conditions, and $Fe(OH)_2(s)$ to $Fe_2(OH)_3Cl(s)$ were detected. Additionally, when $Fe_2\,(OH)_3Cl(s)$ was added to sodium sulfate brines, the formation of green rust (II) sulfate was observed, along with the generation of hydrogen gas [Nemer 2011].

The presence of Cl^- interferes with the formation of $Fe(OH)_2$ through a competition between OH^- and Cl^- ions in the initial oxidation of Fe [Ashley and Burstein 1991; MacFarlane and Smedley 1986]. Thus, a mixed Cl^- /OH^- layer forms [Ashley and Burstein 1991], which would be expected to interfere with the formation of a passive $Fe(OH)_2$ layer or its transformation to Fe_3O_4. Consequently, aqueous and solid iron species anticipated in the repository include iron metal, solid ferrous hydroxide [$Fe(OH)_2•xH_2O(s)$], iron sulfides (such as mackinawite [$FeS_{(s)}$]), aqueous ferrous iron [Fe^{2+}], green rust that can contain several different anions in its structure (Cl^-,SO_4^{2-} or NO^{3-}), and magnetite.

In the expected scenario, the redox conditions of the repository are defined primarily by the iron corrosion products due to the predominance and reactivity of container and waste material in the brine. It is accepted that the initial corrosion of metallic iron (and that of iron present in steel) under anoxic conditions produces in the medium- to long-term a mixed magnetite type Fe(II)-Fe(III) spinel. Magnetite ($Fe_3O_{4(s)}$) is therefore considered as the most likely solid phase to form. It is the anoxic corrosion product of steel and iron used in most assessments evaluating the evolution of the redox conditions in underground repositories for radioactive waste [see for example, Duro et al. 2014; Schramke et al. 2020].

There is a large body of work examining Pu redox and solubility behavior in acidic and neutral solutions under relatively low ionic strength conditions (<1M). However, very limited data are available under alkaline to hyperalkaline conditions and under high ionic strengths. As part of the WIPP project, Felmy et al. (1989) investigated the solubility of $Pu(OH)_{3(am)}$ containing Fe^0 powder in deionized water and two synthetic brines: the Permian Basin Brine (PBB)1 (I ~ 6 M mainly NaCl brine) and PBB3 (I ~ 10 M Na-Mg-Cl brine). The measured solubility of $Pu(OH)_3$ is several orders of magnitude higher in brines than in deionized water at the same hydrogen ion concentration.

$$Pu(OH)_3(am) \Leftrightarrow Pu^{+3} + 3OH^- \ (\log K_{sp} = -26.2 \pm 0.8\ )$$

Solvent extraction results obtained from the aqueous phase showed ~90% Pu(III/IV) for deionized water. The percent of aqueous Pu(III) in brines ranged from 69-95%, with the majority of measurements above 90%. The solids were not characterized [Felmy et al. 1989].

Fujiwara et al. (2001) measured the solubility of $PuO_2•xH_2O$ from oversaturation in the pH range from 4 to 9 at 25 °C in 1.0 M $NaClO_4$ solution containing $Na_2S_2O_4$ as a reductant. The solid phase was attributed to $PuO_2·xH_2O$ by color and the solubility measurements, as well as UV/Vis spectrophotometry data indicating the presence of Pu(III) at pH < 6. This study calculated a log K_{sp} = -38.39 ± 0.19 at I=1.0; a value much lower than that measured by [Felmy et al. 1989; Fujiwara 2001].

Altmaier et al. (2009) studied the solubility of Pu(IV) hydrous oxide at 22±2 °C under an Ar atmosphere in 0.25 and 3.5 M $MgCl_2$ and 3.5 M $CaCl_2$ (presence and absence of metallic iron powder). In alkaline 3.5–4.0 M $CaCl_2$, ternary Ca-Pu-OH complexes are formed and the solubility of $PuO_2{\cdot}xH_2O_{(s)}$ increases from about 10^{-10} M at pH=11 to 10^{-8}–10^{-7} M at pH=12, both in the presence and absence of Fe powder. In the presence of iron, the aqueous speciation is dominated by Pu(III) at pH<10 and by Pu(IV) complexes at pH>10. In the absence of reducing agents, the aqueous speciation is dominated by Pu(V), with significant contributions of Pu(IV) complexes at pH>10. Solubilities measured under these conditions were significantly higher than predicted if no reduction to Pu(III) was being observed. The Pu concentrations were around 10^{-8} M in the 3.5 M $MgCl_2$ with about two orders of magnitude attributed to the increased ionic strength of the brine [Altmaier et al. 2009]. Altmaier et al. (2013) extended the previous work to investigate the effects of carbonate on the oxidation state of Pu in strongly reducing brine solutions. In the carbonate-containing sample, the Pu(III) concentration in solution remained high at $10^{-5.4}$ M even after 582 days of equilibration. XANES analysis performed at the end of the experiments showed a Pu(III) solid phase. This unexpected finding was explained by the potential stabilization of Pu(III) in the solid phase by coordination with carbonate ligands in a strongly saline environment [Altmaier et al. 2009; Altmaier et al. 2013].

A more recent study by Tasi et al. (2018) investigated the solid phase controlling the $^{242}PuO_{2(am,hyd)}$ solubility at pH = 9 and 12 in 0.1 M NaCl in the presence of Sn(II) (pe + pH= 2). XANES/EXAFS measurements were performed after 146 days of contact time. The authors reported the presence of $Pu(III)_{(s)}$ together with $Pu(IV)_{(s)}$ at pH= 9 and 12, although the aqueous Pu concentration remained in the 10^{-11} M range, which implied that the concentration was being defined by the solubility limit of PuO_2(am,hyd) in equilibrium with $Pu(OH)_{4(aq)}$ [Tasi et al. 2018].

The expected scenario for the WIPP is that the repository will remain sealed and unsaturated throughout its 10,000-year performance lifetime. It is only through low-probability human intrusion scenarios that brine inundation of the waste is predicted to occur and it is only these intrusion scenarios that lead to the potential for direct brine release (DBR) from the WIPP. The environmental chemistry and speciation (oxidation state, complexation, and colloid formation) of Pu is important because of the need to define the actinide source term for these DBR release scenarios in the WIPP performance assessment (PA). The oxidation state of Pu in the WIPP environment has been a topic of interest since the initial CCA. Pu was initially expected to be present primarily as Pu(IV), but since the presence of Pu(III) could not be ruled out, it was also included in PA calculations. This led to a position in PA calculations that is commonly referred to as “Pu(III) in 25 % and Pu(IV) in % 75”. This study aims to investigate the solubility of Pu under the expected WIPP conditions and to determine the oxidation state of the solid phase that will control the solubility.

2.0 EXPERIMENTAL

2.1 Chemicals

NaCl, HNO_3, NaOH, HCl, $NaHCO_3$, $MgCl_2\cdot 6H_2O$ $CaCl_2\cdot 2H_2O$ $Na_2B_4O_7\cdot 10H_2O$, LiCl, KCl, NaBr, Na_2SO_4 (Fisher Scientific), HBr, oxalate [disodium oxalate], EDTA [disodium EDTA$\cdot 2H_2O$] (Sigma-Aldrich), citrate [citric acid anhydrous] (Fluka), acetate [acetic acid], (Acros Organics) were used in this study. All solutions were prepared with high purity water (HPW, 18.2 MΩ·cm). All solutions and samples were prepared by first degassing of HPW with nitrogen for 5-6 hours and then handled inside an inert gas (nitrogen) glovebox at 24 ± 2 °C. All brine preparations, final Pu stock preparations, experimental setup, and sampling were conducted in a nitrogen atmosphere glovebox. Samples remained in the glovebox for the duration of the experiments. Oxygen partial pressure was kept below 10 ppm throughout the experiments. Samples were doubly contained in sealed vessels to prevent any exposure to oxygen and prevent sample evaporation. Also, dissolved oxygen was measured with a Rhodazine test kit (CHEMetrics made in USA) (detection limit of 25 ppb) and found to be below detection limit.

2.2 Brine Solutions

The predicted range in brine composition expected in the WIPP is shown in Table 1. These brines are Na/Mg/Cl dominated with lesser amount of calcium, borate, sulfate, potassium, lithium, bromide, and carbonate. In long term experiments, 90% strength compositions are used to prevent salt precipitation and minimize mineral colloid and pseudo-colloid formation. This dilution is a necessary step for anoxic experiments. The 30 mL polypropylene bottles were conditioned with brine solutions for 2 weeks before experiments began.

Table 1. Concentrations of WIPP brine components used in Pu solubility experiments.

Ion	90% GWB* (M)	90% pC_{H+} 9 ** (M)	90% pC_{H+} 10*** (M)
Li^+	3.89E-03	3.38E-03	3.21E-03
Na^+	3.13E+00	3.15E+00	4.13E+00
Mg^{2+}	9.01E-01	9.27E-01	1.05E-01
K^+	4.14E-01	4.12E-01	4.05E-01
Ca^{2+}	1.22E-02	1.22E-02	1.21E-02
Cl^-	4.96E+00	4.89E-02	4.82E+00
SO_4^{2-}	1.57E-01	1.58E-01	1.52E-01
Br^-	2.36E-02	2.12E-02	2.11E-02
$B_4O_7^{2-}$	3.49E-02	3.50E-02	2.49E-03

*GWB: Generic Weep Brine.
** pC_{H+} 9: Specific brine at pH 9.
***pC_{H+} 10: Specific brine at pH 10.

2.3 ^{239}Pu Stock Solution

^{239}Pu obtained from Oak Ridge National Laboratory in oxide form (PuO_2 (plutonium(IV) oxide)) with black powder (Batch Pu-239-1T96) with ^{239}Pu % 97.383 and ^{240}Pu < % 2.611, ^{241}Pu % 0.002 purity. PuO_2 black powder was dissolved in concentrated HNO_3 and 5 µL HF at 70 °C in a Teflon vial. The Pu solution in concentrated HNO_3 was then heated to dryness at approximately 200 °C in a Teflon vial on a hot plate. Five mL of 1 M HCl was added to the dried Pu solution and evaporated several times at 200 °C. Pu(III) was prepared with concentrated hydrobromic acid (HBr) at 120 °C. The residual solid was dissolved in HPW to produce a Pu(III) stock solution. Pu(IV) was prepared through the addition of 6 M nitric acid (HNO_3) to the Pu(III) solid from the previous preparation and taken to dryness. This solid was resuspended in 1 M HCl to produce a Pu(IV) stock solution. The oxidation state purity of this solution was confirmed by UV-vis spectroscopy. Spectrophotometric measurements were performed using a Cary 5000 (Varian) UV-VIS-NIR spectrometer in double-beam mode. Measurements were conducted in gas-tight cuvettes. Spectra were recorded with a 0.2 nm data interval, a scan rate of 60 nm•min^{-1} and a slit-width of 0.6 nm. Pu(III) and Pu(IV) UV-Vis spectra are shown in the Appendix.

$Pu(OH)_3$(am) and $Pu(OH)_4$(am) were prepared by adding an aliquot of the Pu(III) or Pu(IV) stock solution to the polypropylene bottles. An equal volume of 50% (weight/weight) carbonate free NaOH (Acros organics) was added to precipitate the blue $Pu(OH)_3$(am) and $Pu(OH)_4$(am) solid.

An Agilent 7900 quadrupole inductively coupled plasma-mass spectrometer (ICP-MS) was used for the determination of total Pu concentration and was calibrated with an external ^{239}Pu standard (Eckert and Ziegler) and indium internal standard (1000 ppm in 2% HNO_3, High Purity Standards).

2.4 Sample Matrix

The mass of ^{239}Pu in each sample was ~2 mg. Commercially available iron powder (Fe^0) (Aldrich) or magnetite (Fe_3O_4) (Aldrich) were added (~100 mg) to create a reducing environment. Both iron minerals were analyzed by powder X-ray diffraction (P-XRD). Measurements were performed using a D8 Discover diffractometer (Bruker AXS, Germany) equipped with a Cu radiation tube (Cu K–alpha = 0.15418 nm, current: 25 mA, voltage: 40 kV), Ni filter and a Sol–X detector before starting the experiments. In addition, after three years, both iron minerals were analyzed once again by XRD after interaction with WIPP salt and ^{239}Pu to check if there was any change in the iron minerals. (All XRD results are shown in the Appendix.) Concentrations of WIPP-relevant organics are acetate: 2.83 x 10^{-2} M, oxalate: 1.13 x 10^{-2} M, citrate: 2.30 x 10^{-3} M, EDTA: 7.92 x 10^{-5} M [Van Soest 2018]. Samples were equilibrated in three synthetic WIPP brines as the background electrolyte with an under-saturation approach: 90 % GWB, 90 % pC_{H+} 9 and 90 % pC_{H+} 10 specific brines. Samples were systematically monitored for pC_{H+} and ^{239}Pu concentration (M) for up to 800-1,100 days. The aqueous concentration of ^{239}Pu was measured by ICP-MS after 10 kDa ultrafiltration (~2–3 nm- Pall-type filters, Omega-modified polyethersulfone) at 13,000 RPM centrifugation for 5 minutes. Table 2 includes a description of the experimental variables including Pu isotope, pC_{H+}, presence or absence of WIPP organics, and iron phase used.

Table 2. Experimental matrix for Pu oxidation state studies.

LANL Experiment Designation	Organics present	Iron phase	Brine type	$[I]_{tot}$ [M]**
^{239}Pu(III)_pH8_Fe^0_1,2	None	Fe^0	90 % GWB	6.34
^{239}Pu(III)_pH9_Fe^0_1,2	None	Fe^0	90 % pC_{H+} 9	6.39
^{239}Pu(III)_pH10_Fe^0_1,2	None	Fe^0	90 % pC_{H+} 10	5.04
^{239}Pu(III)_pH8_magnetite_1,2	None	Fe_3O_4	90 % GWB	6.34
^{239}Pu(III)_pH9_magnetite_1,2	None	Fe_3O_4	90 % pC_{H+} 9	6.39
^{239}Pu(III)_pH10_magnetite_1,2	None	Fe_3O_4	90 % pC_{H+} 10	5.04
^{239}Pu(III)_pH8_Fe^0_Org_1,2	all organics*	Fe^0	90 % GWB	6.34
^{239}Pu(III)_pH9_Fe^0_Org_1,2	all organics*	Fe^0	90 % pC_{H+} 9	6.39
^{239}Pu(III)_pH10_Fe^0_Org_1,2	all organics*	Fe^0	90 % pC_{H+} 10	5.04
^{239}Pu(III)_pH8_magnetite_Org_1,2	all organics*	Fe_3O_4	90 % GWB	6.34
^{239}Pu(III)_pH9_magnetite_Org_1,2	all organics*	Fe_3O_4	90 % pC_{H+} 9	6.39
^{239}Pu(III)_pH10_magnetite_Org_1,2	all organics*	Fe_3O_4	90 % pC_{H+} 10	5.04
^{239}Pu(III)_pH8_1,2	None	No	90 % GWB	6.34
^{239}Pu(III)_pH9_1,2	None	No	90 % pCH+ 9	6.39
^{239}Pu(III)_pH10_1,2	None	No	90 % pCH+ 10	5.04
^{239}Pu(IV)_pH8_1,2	None	No	90 % GWB	6.34
^{239}Pu(IV)_pH9_1,2	None	No	90 % pCH+ 9	6.39
^{239}Pu(IV)_pH10_1,2	None	No	90 % pCH+ 10	5.04

* Acetate: 2.83×10^{-2} M, oxalate: 1.13×10^{-2} M, citrate: 2.30×10^{-3} M, ethylenediaminetetraacetic acid (EDTA): 7.92×10^{-5} M [Van Soest 2018].

** Ionic strength calculated via the EQ3/6 software program [Wolery 2008] using Sandia National Laboratories FMT database [Xiong 2011].

2.5 pH and E_h measurement

pH measurements were taken with a Ross semi-micro combination electrode and an Orion 3 Star meter. The hydrogen ion concentration (pC_{H+}= –log [H+], in molar units) was determined according to $pC_{H+} = pH_{exp} + \Delta pH$ as described previously in the literature [Altmaier et al. 2003; Borkowski et al. 2009] where pH_{exp} is the measured pH value and ΔpH is the empirical correction factor entailing the liquid junction potential of the electrode and the activity coefficient of H^+. The pC_{H+} of the prepared WIPP brines are stable. Over the course of between 800-1,100 days, pC_{H+} in most samples was within half a pH unit of the initial pC_{H+}. Some of the samples had changes in pC_{H+} that were over 1 pH unit higher than the initial value. Table 3 shows the shift in pC_{H+} as a function of time over the duration of these solubility experiments. Oxidation-reduction potential measurements were obtained using an Orion A221 meter equipped with a Mettler Toledo InLab glass redox microelectrode with a platinum ring. Corrections from redox potential to E_h were made by adding the Ag/AgCl redox potential from the meter reading Zobel solution (LabChem). In E_h measurements, especially in solutions with high ionic strength, the uncertainty can be up to 200 mV. In order to perform more precise measurements and reduce the error, after each E_h measurement the electrode was washed with 1 M HCl, then water, then 1 M NaOH, and the final wash with water (total cleaning process time is 1-2 hours), and after every two or three measurements the electrode filling solution, 3 M KCl, was replaced with fresh solution [Altmaier et al. 2010]. E_h values are shown in Table 3.

Table 3. pC_{H+} and E_h(mV) value as a function of days.

LANL Experiment Designation	**pC_{H+} value in days**					**E_h (mV)**
	21	28	103	205	800	800 days
^{239}Pu_pH8_magnetite_Org_1	8.04	8.05	8.12	8.24	8.60	82
^{239}Pu_pH8_magnetite_Org_2	7.95	8.09	8.13	8.35	8.50	32
^{239}Pu_pH9_magnetite_Org_1	8.97	9.13	9.13	9.34	9.20	68
^{239}Pu_pH9_magnetite_Org_2	9.01	9.07	9.14	9.25	9.00	112
^{239}Pu_pH10_magnetite_Org_1	9.96	10.12	9.70	9.83	9.70	95
^{239}Pu_pH10_magnetite_Org_2	9.94	10.01	9.57	9.86	9.50	127
^{239}Pu_pH8_magnetite_1	8.04	8.05	8.12	8.24	8.20	268
^{239}Pu_pH8_magnetite_2	7.95	8.09	8.13	8.35	8.10	245
^{239}Pu_pH9_magnetite_1	8.97	9.13	9.13	9.34	9.20	291
^{239}Pu_pH9_magnetite_2	9.01	9.07	9.14	9.25	9.10	269
^{239}Pu_pH10_magnetite_1	9.96	10.12	9.70	9.83	9.30	309
^{239}Pu_pH10_magnetite_2	9.94	10.01	9.57	9.86	9.20	300
^{239}Pu_pH8_Fe^0_Org_1	8.06	8.05	8.25	8.28	8.30	-357
^{239}Pu_pH8_Fe^0_Org_2	8.06	7.93	8.27	8.30	8.20	-335
^{239}Pu_pH9_Fe^0_Org_1	9.08	9.05	9.21	9.26	9.20	-325
^{239}Pu_pH9_Fe^0_Org_2	9.06	9.08	9.17	9.18	9.00	-300
^{239}Pu_pH10_Fe^0_Org_1	10.18	10.11	9.94	9.90	10.10	-437
^{239}Pu_pH10_Fe^0_Org_2	10.14	10.03	9.95	9.91	9.80	-380
^{239}Pu_pH8_Fe^0_1	8.05	8.01	8.97	8.96	8.50	-366
^{239}Pu_pH8_Fe^0_2	8.01	8.03	8.51	8.53	8.30	-350
^{239}Pu_pH9_Fe^0_1	9.05	9.00	9.23	9.21	9.50	-335
^{239}Pu_pH9_Fe^0_2	9.02	8.9	9.2	9.16	9.40	-366
^{239}Pu_pH10_Fe^0_1	10.06	9.89	9.34	9.74	9.60	-367
^{239}Pu_pH10_Fe^0_2	10.00	9.93	9.66	9.75	9.50	-422

2.6 Characterization of solid phase: XAS (X-Ray Absorption Spectroscopy)

To understand the Pu oxidation state distribution from ongoing solubility experiments in synthetic WIPP brine with iron corrosion products about 800 days, two different phases in the sample vials were separated from each other using a magnet: (1) Pu sorbed to the iron corrosion products (Fe^0 or magnetite) and (2) Pu precipitates. Figure 1 shows illustrations of XAS sample preparation. These separated phases were placed in XAS sample holders (triple contained aluminum holders, Kapton windows, and indium wire seal), sealed inside an anoxic containment vessel purged with nitrogen gas, and sent to beamline 11-2 at Stanford Synchrotron Radiation Light Source (SSRL) for Pu-L_{III} edge analysis. Beamline 11-2 was equipped with a 26-pole and 2.0 tesla wiggler, utilizing a liquid nitrogen-cooled double-crystal Si(220) monochromator, and employed collimating and focusing mirrors. The sample holders were loaded into a liquid nitrogen cryostat (Kapton windows; 2 mm) and placed under vacuum (10^{-7} Torr) prior to starting measurements. The cryostat was attached to the beamline 11-2 XAS rail, equipped with three ionization chambers through which nitrogen gas was continually flowed, thereby reducing thermal disorder and preventing beam-induced oxidation state changes.

The Pu-L_{III} edge (18.057 keV) measurements were conducted in fluorescence mode using a 100-element solid state Ge detector (Canberra). A Ti filter was placed in front of the detector to remove scatter from the sample. A Zr foil was placed “downstream” of the sample to calibrate during each sample scan with the intent of providing in situ calibration. The Zr-K edge calibration was performed at E_0 = 17997.6 eV. Spectra were calibrated, and the XANES data analysis was performed with the LARCH software program in version 0.9.81., where the average oxidation state of Pu in the bulk EXAFS samples was determined by fitting the XANES region between 18025 and 18150 eV using a linear combination fit of reference spectra for Pu(III) and Pu(IV). LCF analysis was performed by using a tool in the software program LARCH [Newville 2013; Schmeide et al. 2006; Martin et al. 2007].

Normalization, transformation from energy into K-space, subtraction of a spline background and shell fits, were performed with LARCH software program to perform the EXAFS analysis [Newville 2013] and FEFF8 [Ankudinov et al. 2002]. The single scattering phases and amplitudes were calculated using the crystal structure of PuO_2 to model Pu-Pu [Belin et al. 2004]. The crystal structure of $(Eu_{0.67}\,Mg_{0.33})_2\,(Ti_2\,O_{6.67})$ was used to model Pu-O interactions by replacing Eu with Pu [Chtoun et al. 1997]. Also, Pu-Fe theoretical scattering paths for this shell fit approach were derived by replacing Fe atoms in magnetite structures by Pu [Glazyrin et al. 2012]. The theoretical models were fit to the K^3-weighted EXAFS spectra using an amplitude reduction factor of S_0^2(k) = 0.9.

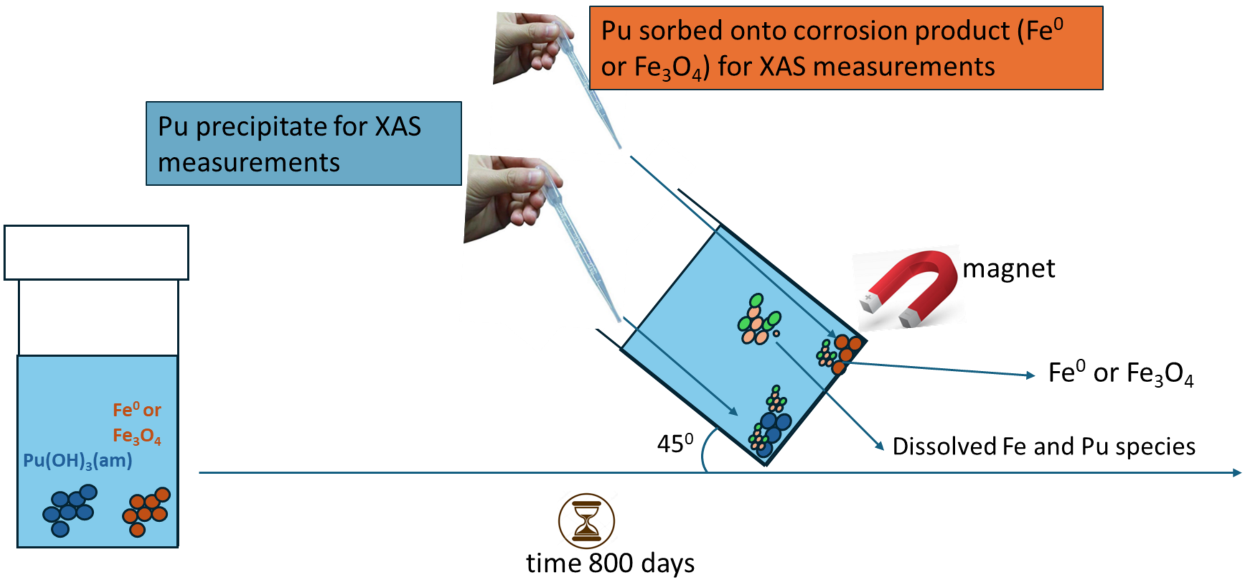

Figure 1: XAS sample preparation.

3.0 RESULTS

3.1 XANES (X-ray Absorption Near Edge Spectroscopy)

Pu-LIII edge XANES spectra were collected from ongoing solubility experiments over a period of approximately three years, in which different iron minerals and organics were present. The most important point of these analyses is that the oxidation state of Pu is determined not only in the Pu precipitate, but also in the Pu adsorbed by corrosion products (magnetite and Fe^0) in the presence and absence of organics.

Pu LIII-edge XANES spectra do not contain pre-edge features that could identify the oxidation state or coordination geometry. The spectra contain only one absorption feature, called the white line (WL). All measured and normalized Pu LIII–edge XANES spectra are shown in Figure 2. The figure also includes reference spectra for Pu(III), Pu(IV), Pu(V) and Pu(VI), where significant shifts to higher energy are observed with increasing oxidation state. Since the WL of the samples obtained from the system containing Fe^0 match the Pu(III) reference, these samples are shown with the same offset as Pu(III). Likewise, the WL of the samples obtained from the system containing magnetite matches the Pu(IV) reference and they are shown with Pu(IV).

Another distinguishing feature of Pu LIII-edge XANES is the presence of a peak near the absorption edge for Pu(V) and Pu(VI) species, indicative of the plutonyl functional group (Figure 2). This makes speciation between Pu(III/IV) and Pu(V/VI) more apparent. It is possible to distinguish between Pu(III) and Pu(IV) species due to the difference in initial energy and WL position. The overall shape of the Pu peak strongly suggests the absence of Pu(VI) and Pu(V) in all analyzed samples.

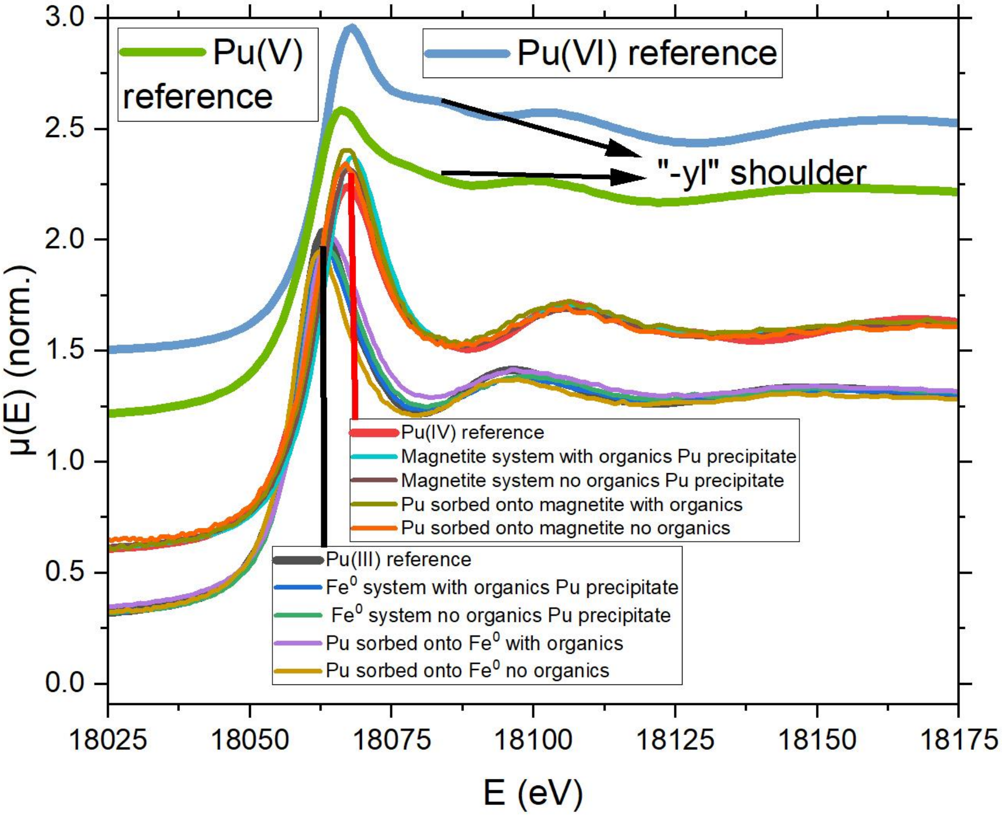

Figure 2. Pu L_{III}–edge XANES spectra obtained from Pu sorbed onto corrosion product (Fe^0 and magnetite) and precipitates including reference spectra for Pu(III), Pu(IV), Pu(V) and Pu(VI).

The WL of the XANES spectra collected for Pu precipitate phases and iron corrosion phases in the presence and absence of organics are listed in Table 4 with Pu(III) and Pu(IV) reference spectra. In samples containing Fe^0, the dominant oxidation state was determined to be Pu(III). This is clearly valid for the oxidation state of Pu on both the metallic iron surface and in the precipitate phase. However, in samples containing magnetite, the Pu(IV) oxidation state was determined on both the surface of the magnetite and in the precipitate phase. While making this evaluation, the energy in the WL, which is like a fingerprint of Pu, was utilized.

Another strategy to determine Pu oxidation state is linear combination fit (LCF) analyses. A linear combination fit using a spectrum from each of these oxidation states can be used to fit the oxidation state of an unknown solid. Pu(III) and Pu(IV) reference spectra were selected to perform LCF analyses. All LCF results are presented in Figures 3 and 4, along with the component spectra and the residual of the fit. The fit range was chosen to cover both the onset energy and the entire absorption feature (18025–18150 eV). The results of the fits are given in Table 4 as a percent Pu(III) and Pu(IV) character of each sample.

Table 4. The White Line (WL, eV) was obtained by Pu L_{III}-edge XANES spectroscopy measurements from investigated Pu-samples. ΔE represents the energy shift between the Pu(III) reference and the measured samples. The results of LCF are given in %.

LANL experiment designation	WL in (eV)	ΔE (eV)-Pu(III) (± 0.5 eV)	Pu(III) in % (± 10%)*	Pu(IV) in % (± 10%)*
Pu sorbed onto Fe^0 no organics	18062.6	0.1	100	0
Pu sorbed Fe^0 with organics	18063.8	-1.1	84	16
Fe^0 system no organics Pu precipitate	18063.8	-1.1	98	2
Fe^0 system with organics Pu precipitate	18063.2	-0.5	94	6
Pu sorbed onto magnetite no organics	18066.9	-4.2	23	77
Pu sorbed magnetite with organics	18067.1	-4.4	10	90
Magnetite system no organics Pu precipitate	18067.6	-4.9	1	99
Magnetite system with organics Pu precipitate	18068.0	-5.3	1	99
Pu(III) [Schmeide et al. 2006]	18062.7	-	-	-

*Pu oxidation state distribution in percentage amount was calculated by LCFA by using Pu(III) and Pu(IV) reference spectra of Pu-L_{III} edge [Schmeide et al. 2006, Martin et al. 2007].

The most important reasons for this are as follows. While the E_h value in the metallic iron system is around -400 mV, the E_h value in magnetite-containing samples varies between +30 and +309, which is more oxidizing. The probability of Pu(V) and (VI) being present at these E_h values, i.e., in a reducing environment, is very low. In addition, when we compare the measured Pu-L_{III} edge XANES spectra with Pu(V) and (VI) XANES spectra, the shoulders created by the dioxide Pu-O bonds are not observed.

EXAFS analyses will be discussed in the next section. No Pu=O_{ax} bond was found in any measured sample at 1.7-1.8 Å. In Pu(V) and Pu(VI) species, there is a Pu=O_{ax} bond at the 1.7-1.8 Å range [Reich et al. 2001]. For the reasons listed above, only Pu(III) and Pu(IV) reference spectra were used in the LCF analysis**.**

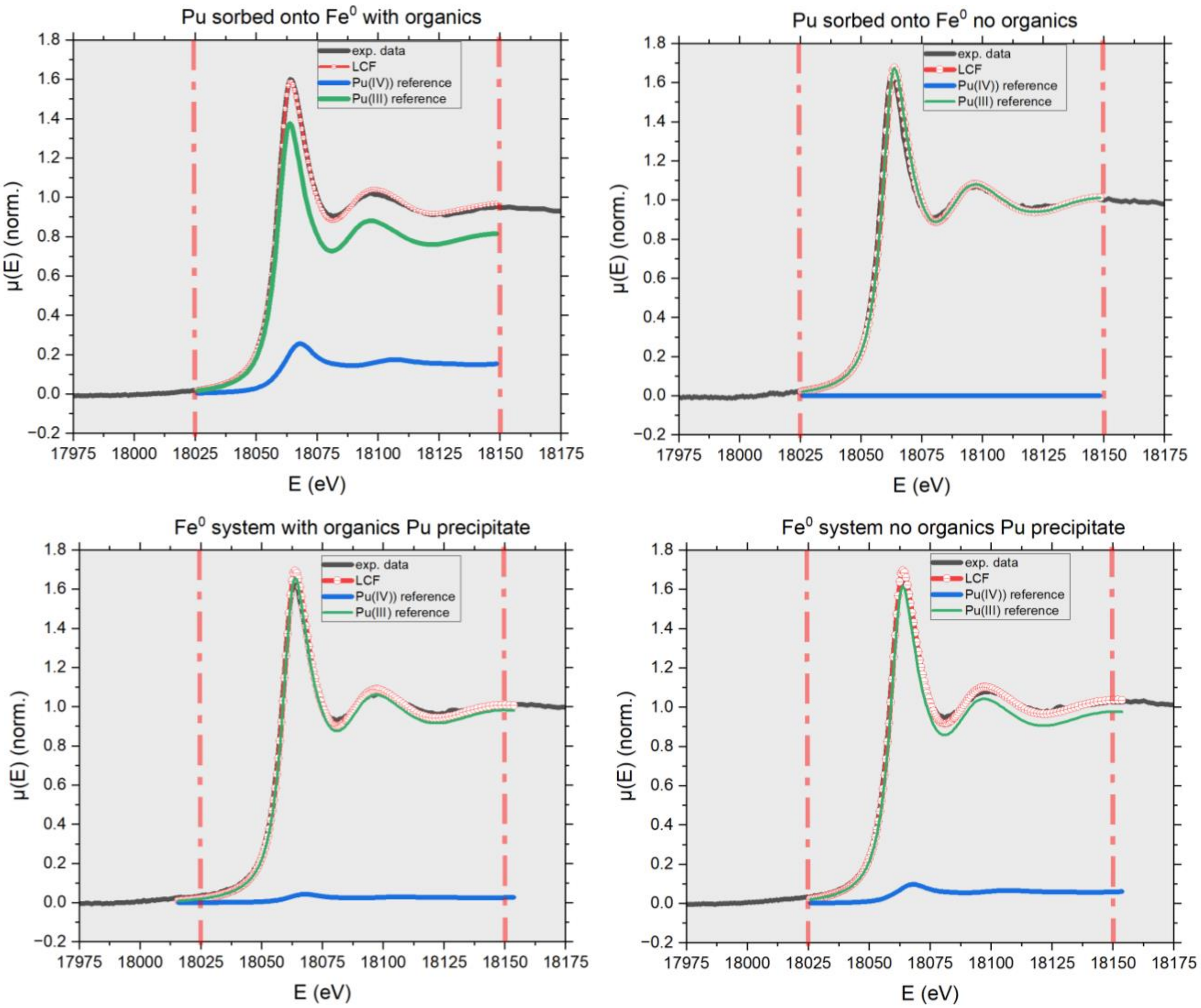

Figure 3. The background subtracted and normalized Pu L_{III}-edge XANES spectra obtained by measuring the solid phase in the solubility experiments in the presence of Fe^{0}and organics are shown together with the corresponding LCF. Experimental data are compared with the corresponding linear combination fits of Pu(III), Pu(IV). The contributions of the individual components are included.

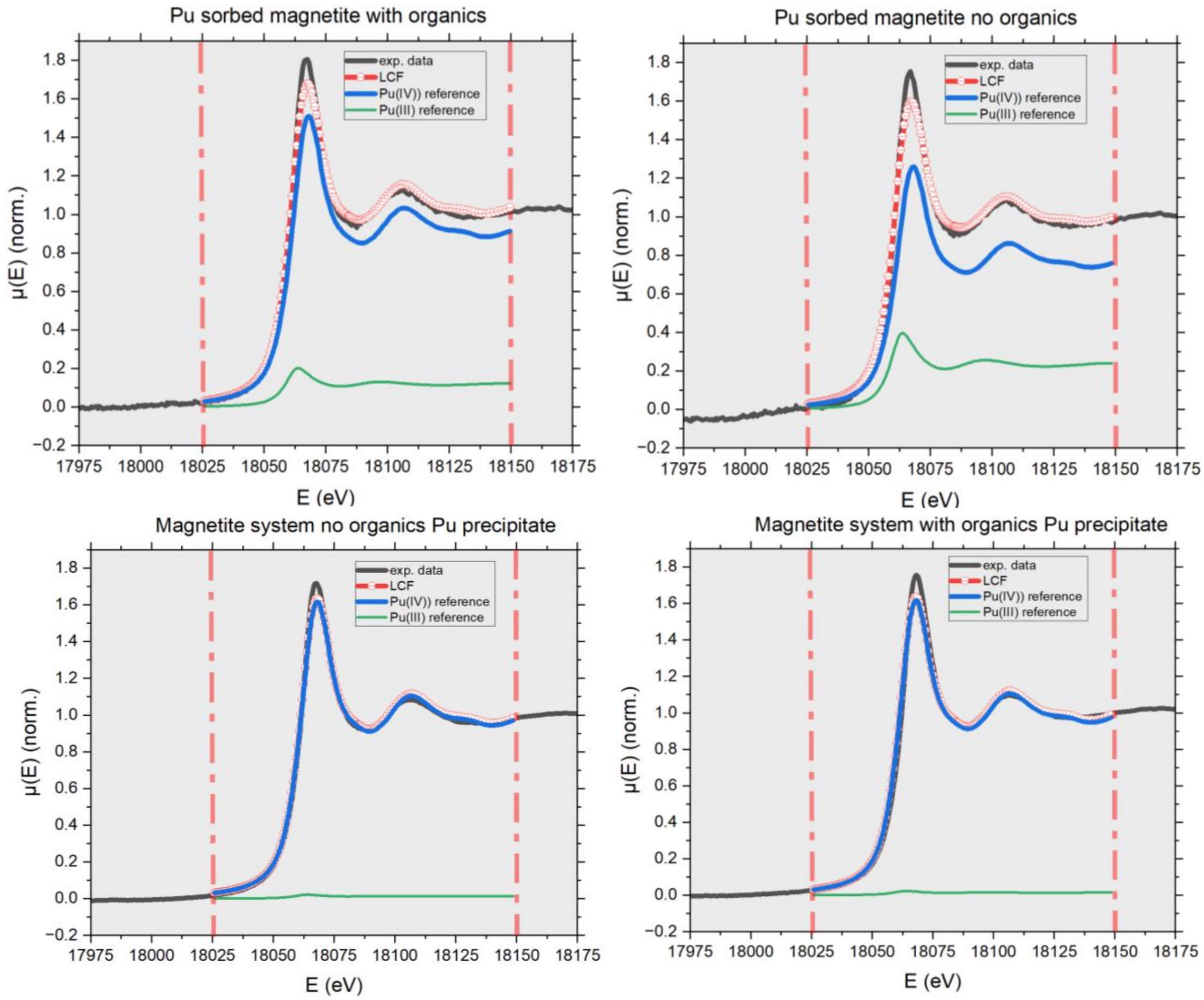

Figure 4. The background subtracted and normalized Pu L_{III}-edge XANES spectra obtained by measuring the solid phase in the solubility experiments in the presence of magnetite and organics are shown together with the corresponding LCF. Experimental data are compared with the corresponding linear combination fits of Pu(III), Pu(IV). The contributions of the individual components are included.

3.2 EXAFS

The initial aim of this study was to investigate the oxidation state of Pu in the presence of two different corrosion products (magnetite and Fe^0) in the presence and absence of organics in synthetic WIPP brine. Since there is a $Pu=O_{ax}$ bond in the range of 1.7-1.8 Å in Pu(V) and Pu(VI) species, EXAFS analyses provide an important opportunity to understand whether Pu(V) or Pu(VI) is present in the analyzed samples. Figure 5 shows Pu L_{III}-edge k^2-weighted EXAFS spectrum (upper) and corresponding Fourier transform magnitude (below) of Pu from ongoing solubility experiments. The samples shown in Figure 4 were analyzed by taking the Pu precipitate portion of the ongoing solubility experiments. Due to the limited accessible k range and the noticeable noise in the experimental data, the chemical identity and relative importance of possible contributions after 4 Angstrom bond distance cannot be determined with certainty.

Based on data in the literature, longer Pu–O interatomic distances correspond to weaker surface complexes (i.e., monodentate) or aquo ions at about 2.3-2.4 Å [Schmeide et al. 2006], while shorter distances correspond to stronger surface complexes, solids or hydroxides group at 2.1-2.2 Å [Dumas et al. 2019; Dardenne et al. 2009].

The first peak in the Fourier transform was successfully modeled using a split oxygen shell, which includes two discrete scattering paths of Pu-O_1 and PuO_2. Pu-O_1 interaction showed with coordination number (CN) between 1-4 Pu-O_1 scatter between 2.10 Å and 2.20 Å bond distance. Similar bond lengths have been reported in the literature for Pu and have been assigned as a pyrochlore-like coordination environment within the structure [Dumas et al. 2019]. Also, the Pu−O_2 fits to a bond length of approximately 2.33–2.42 Å, suggesting the presence of coordinated water around the Pu atom [Reich et al. 2001; Reich et al. 2007].

The second peak at about 3 Å in non-phase-corrected R-space was modeled with 3 Pu–Fe shell at about 3.40 Å. These distances are similar to the ~3.37 Å Fe–Fe distance of corner-sharing octahedra in the hematite structure and similar to An–Fe distances found in other studies [Li et al. 2016; Stagg et al. 2022; Hu et al. 2010].

In addition to this speciation, a Pu–Pu scattering contribution at longer distances of 3.7 angstroms was observed in EXAFS data of the precipitate phase, which is due to PuO_2 precipitation, which is mostly coordinated by a single shell of 8 O atoms at ∼2.36 Å and 12 Pu at 3.82 Å [Balboni et al. 2020]. In the case of the sample from the Fe^0 system with organics, there is no evidence of the formation of polynuclear Pu-Pu species in the EXAFS spectra. In the FT (Fourier Transform) obtained from measured data, a small peak is visible at about = 3.7 Å, which could possibly be interpreted as Pu–Pu interaction. However, this is not a real effect, but rather caused by noise spectra. Therefore, within the detection limit of the technique, the formation of polynuclear Pu species can be excluded. The clear identification of multiple Fe scatterers in the EXAFS data confirms that the Pu forms a second precipitation complex with Fe.

Table 4 lists a summary of the molecular structure information obtained by the EXAFS fit. Furthermore, a possible interaction between Pu and C was not observed in the Fourier transforms, because carbon atom is generally a relatively weak photoelectron scatterer, which results in weak XAS contributions.

Dumas et al. (2019) found that under certain experimental conditions, Pu(V) in a mixed solution of Fe(II) and Fe(III) was rapidly reduced to Pu(III). Moreover, molecular structure analysis with EXAFS showed a pyrochlore-like coordination environment (split 8-fold oxygen coordination shell with Pu-O distances of 2.22 and 2.45 Å and edge-sharing connection to Fe-octahedra with Pu-Fe distances of 3.68 Å) embedded in the magnetite matrix (Pu-Fe distances of 3.93, 5.17 and

5.47 Å). This suggests that the partial incorporation is due to the structural incompatibility of the large Pu(III) ion for the octahedral Fe site in magnetite.

The presence of Pu-Fe scatterers in the fits to the EXAFS data clearly indicates that Pu is directly associated with dissolved iron or Pu rather than with brine components.

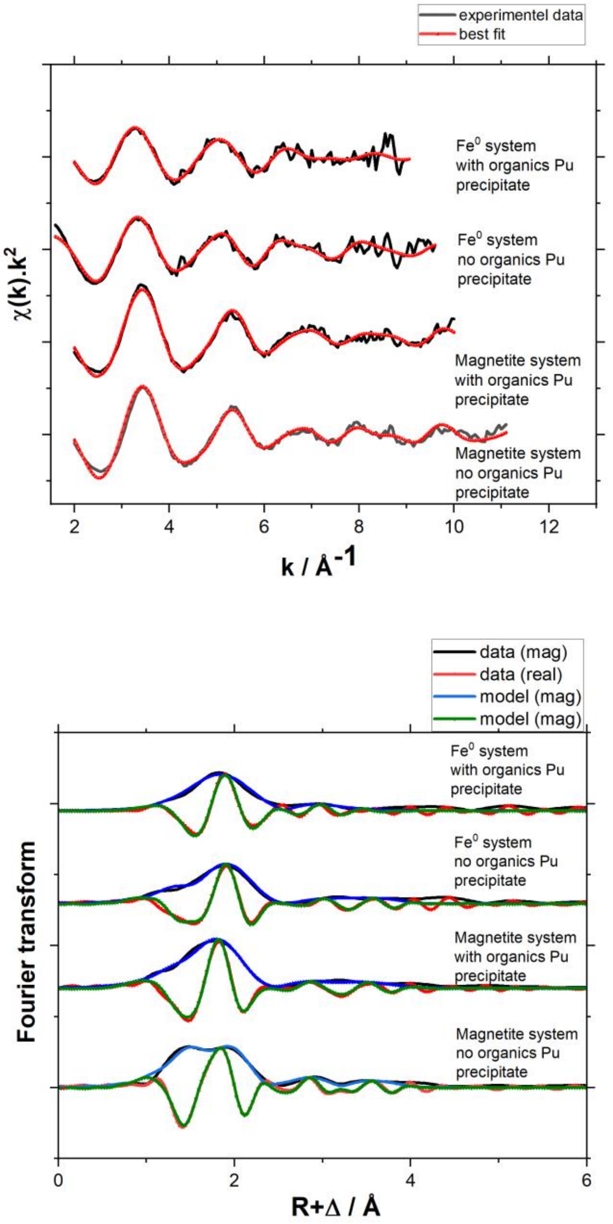

Figure 5. Upper panel: Pu L_{III}-edge EXAFS spectra with exp. data and best fit of investigated samples. Below panel: Corresponding EXAFS Fourier transforms, data magnitude (mag) (black), model magnitude (blue), data real part (red) and model real part (green).

Table 5. Best-fit of Pu L_{III}–edge EXAFS model parameters for magnetite and Fe^0 systems in the presence and absence of organics (S_0^2(k) = 0.9 fixed).

Experiment designation	**Shell**	**CN**	**R [Å]**	**σ^2/[Å^2]**	**Reduced Error**	**ΔE0**
Magnetite system no organics Pu precipitate (k range: 2 – 11.1)	Pu-O$_1$	4.30 +/- 0.58	2.17 +/- 0.01	0.007*	0.025	2.5+/- 0.7
	Pu-O$_2$	7.01 +/- 1.32	2.39 +/- 0.01	0.006 +/- 0.02		
	Pu-Fe	3.0*	3.37 +/- 0.02	0.018 +/- 0.003		
	Pu-Pu	2.33 +/- 1.33	3.68 +/- 0.02	0.009 +/- 0.005		
Magnetite system with organics Pu precipitate (k range:2 - 10.0)	Pu-O$_1$	0.90 +/- 0.32	2.02 +/- 0.03	0.007*	0.019	2.6 +/- 0.9
	Pu-O$_2$	9.23 +/- 1.53	2.33 +/- 0.01	0.018 +/- 0.02		
	Pu-Fe	3.0*	3.42 +/- 0.05	0.021 +/- 0.008		
	Pu-Pu	4.51 +/- 2.15	3.67 +/- 0.02	0.020 +/- 0.01		
Fe^0 system no organics Pu sediment(k range: 1.6 - 9.6)	Pu-O1	1.54 +/-0.45	2.11 +/- 0.03	0.007*	0.051	3.5 +/- 1.2
	Pu-O2	9.12 +/- 1.81	2.42 +/- 0.01	0.015+/- 0.0001		
	Pu-Fe	3*	3.58 +/- 0.04	0.021+/- 0.0001		
	Pu-Pu	1.60 +/- 0.74	3.70 +/- 0.04	0.009 +/- 0.002		
Fe^0 system with organics Pu precipitate (k range: 2-9.0)	Pu-O$_2$	8.15 +/- 1.05	2.44 +/- 0.01	0.019 +/- 0.02	0.04	5.4 +/- 0.8
	Pu-Fe$_1$	3*	3.52 +/- 0.02	0.019 +/- 0.02		
[Smith et al. 2019]	Pu-O	8*	2.34 ± 0.01	0.014 ± 0.001	0.014	5.64
fresh sample	Pu-Fe	4*	3.34 ± 0.02	0.018 ± 0.003		
[Smith et al. 2019]	Pu-O	8*	2.29 ± 0.02	0.018 ± 0.001	0.016	5.31
aged sample	Pu-Fe	4*	3.34 ± 0.02	0.018 ± 0.003		

*Parameter fixed at constant value during fit.

3.3 Solubility

Log[Pu] (M) solubility values in the different WIPP brine in the presence and absence of organics and iron corrosion products (Fe^0 and magnetite) are shown in Figure 6a. Under these conditions, the solubility of Pu changes by up to three orders of magnitude. The spread in solubility data is highest at $pC_{H+} = 9$. A similar scattering is reported by Felmy et al. (1989) for the solubility of Pu(III) in high ionic strength brine solution in the presence of Fe^0 [Felmy et al. 1989]. This can be explained by the fact that the chemistry of Pu and iron is very complex in the neutral pH range and more than one phase can exist simultaneously, e.g., Fe-organic, organic-brine components-Pu or Pu-Fe or Pu-colloid [DiBlasi et al. 2022; Altmaier et al. 2009; Dumas et al. 2019; Micheau et al. 2020; Cobas and Søgaard 2022].

In the solubility studies initiated with Pu(IV) in simple brine systems reported in the literature, Pu concentration could not be measured because it was below the detection limit at neutral or alkaline pH values or very close to the detection limit [Tasi et al. 2018]. Similar trends were observed by Altmaier et al. (2009) as shown in Figure 6b. In two separate experiments initiated with Pu(III) and Pu(IV), although they used the same concentration of background electrolyte and the same reducing agent, the Pu(IV) concentration was close to the detection limit, while in the experiments initiated with Pu(III), the Pu concentration in the liquid phase was two orders of magnitude higher [Altmaier et al. 2009]. We observed the same trend in the experiments initiated with Pu(III) and Pu(IV) in WIPP brine. The solubility of the Pu(III) is about two orders of magnitude higher than that of Pu(IV). This indicates that Pu(III) can be stable in the liquid phase without changing the oxidation state. Altmaier et al. (2009) and Felmy et al. (1989) investigated the oxidation state of Pu in the liquid phase in systems containing reducing iron agents (Fe^0), they reported that Pu(III) was dominant in the liquid phase [Altmaier et al. 2009; Felmy et al. 1989].

The solubility of Pu in $MgCl_2$ brine increases with increasing Mg^{2+} concentration (from 0.25 to 3.5 M) in the presence of Fe^0 [Altmaier et al. 2009]. Considering that the total ionic strength of WIPP brine is higher than the studies conducted by Altmaier et al. (2009), this explains the high Pu concentration in high ionic strength WIPP brine studies. In this study, no significant relationship was established between the presence of organics in the system and Pu solubility in the magnetite system and Fe^0 system. The possible reasons can be explained by the EXAFS results, as the EXAFS analysis showed in the solubility controlling solid phase, Pu is more prone to complex with Fe than bond with C. In addition, complexes form between divalent salt components (Ca^{2+}, Mg^{2+}) or complexes with Fe^{2+} in solution with organics have been reported in the literature [Cobas and Søgaard 2022; Serne et al. 2002].

Rai et al. (2008) experimentally evaluated the solubility of PuO_2(am) in the presence of ferrihydrite and EDTA in dilute solutions from pH 2.3 to 11.5. The measured total Pu concentrations in these experiments were much higher than predicted based on the complexation of Pu(IV) and Fe(III) by EDTA. Oxidation state analysis by solvent extraction showed that significant amounts of Pu(III) were in solution below about pH 8 and Pu(V) or Pu(VI) was in solution above about pH 8.

Reduction of Pu(IV) to Pu(III) in the absence of an added reductant was attributed to reaction with small amounts of ferrous iron in the ferrihydrite. Rai et al. (2008) concluded from their experimental data and calculations that the importance of Pu(IV)-EDTA complexes had been overstated and that Pu(III)-EDTA complexes may play an important role in Pu mobility in reducing environments [Rai et al. 2008].

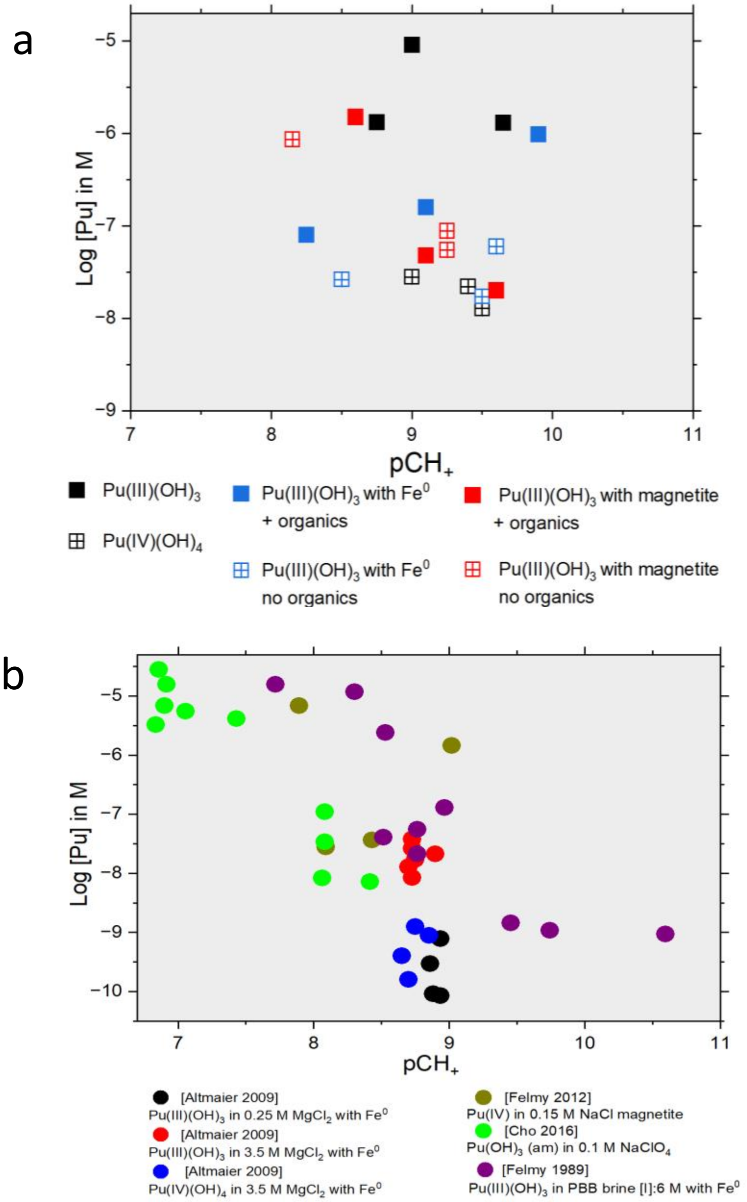

Figure 6. a-) Log[Pu] solubility value in the different WIPP brine in the presence and absence of organics and iron corrosion products (Fe^0 and magnetite), the results obtained had a maximum error of ± 15 %, b-) The experimental solubility data reported in the literature for Pu in alkaline system.

The presence of solid Pu(III) phase was detected in alkaline systems by XANES analysis in relatively new studies: 1) in the presence of carbonate and Fe^0, 2) under very reducing conditions provided by Sn(II) in 0.1 M NaCl [Tasi et al. 2018; Altmaier 2013]. All of these studies and current thermodynamic data confirm the complexity of the Pu(III)/Pu(IV) redox chemistry in the neutral to alkaline pH range. This emphasizes the need for further experiments as a function of pH, reducing conditions and ionic strength, as well as radiolysis which will affect the oxidation state of Pu in favour of Pu(III) or Pu(IV).

Xia et al. (2001) conducted similar experiments of up to 72 days with ERDA-6 brine (Energy Research and Development Administration Well 6, a synthetic brine representative of fluids in Castile brine reservoirs), ^{239}Pu(VI), and metallic iron powder and found that dissolved Pu concentrations were not reduced at $pC_{H+} \geq 9$; measured E_h values were between +470 and +670 mV, and 85% to 90% of the dissolved Pu was present in solution as Pu(V) [Xia et al. 2001]. However, the E_h values in our brine solutions were below +309 mV for magnetite and -437 mV for Fe^0, (see Table 3) which indicates, based on the Pourbaix diagrams, that the Pu species expected in solution are Pu(IV) or Pu(III) (see Figure 7).

4.0 ENVIROMENTAL IMPLICATIONS

The oxidation state distribution and solubility of Pu were investigated in detail in the presence and absence of two different corrosion products and presence and absence of four organics in alkaline WIPP brine solution. To better understand the possible WIPP scenario, two different corrosion products were used to simulate high and low E_h values. In the magnetite containing systems, the dominant oxidation state is Pu(IV) and E_h values are higher, while in the metallic iron containing systems, the dominant oxidation state is Pu(III) and this provides lower E_h values. It was observed that the presence or absence of organics in the system does not affect the oxidation state of Pu as strongly as the corrosion products and this Pu(III) and Pu(IV) ratio remains only in the range of 10-20%. This shows us how important the selection of the most probable corrosion product is to the WIPP conceptual model.

To better understand the Pu speciation, it is very important to understand the speciation of iron in the system. The iron chemistry of the WIPP is crucial to setting the E_h of the repository. Iron has multiple possible fates. The first is conversion to pyrite (FeS_2) through reaction of iron with hydrogen sulfide, which is the byproduct of sulfate-reducing microbial activity that is assumed to occur in the closed repository. Another possibility is the formation of magnetite (Fe_3O_4) through continued reaction with oxygen gas and corrosion from intruding brine. Pyrite is expected to be thermodynamically stable under very reducing E_h conditions. If pyrite formation is suppressed, magnetite is stable over a wide range of E_h values, including those at the water reduction line and under oxidizing conditions ($E_h > 0$) (Figure 7). The red lines represent the calculated Fe Pourbaix diagram. The black arrow indicates the most representative E_h boundaries for WIPP calculations [Reed et al. 2020].

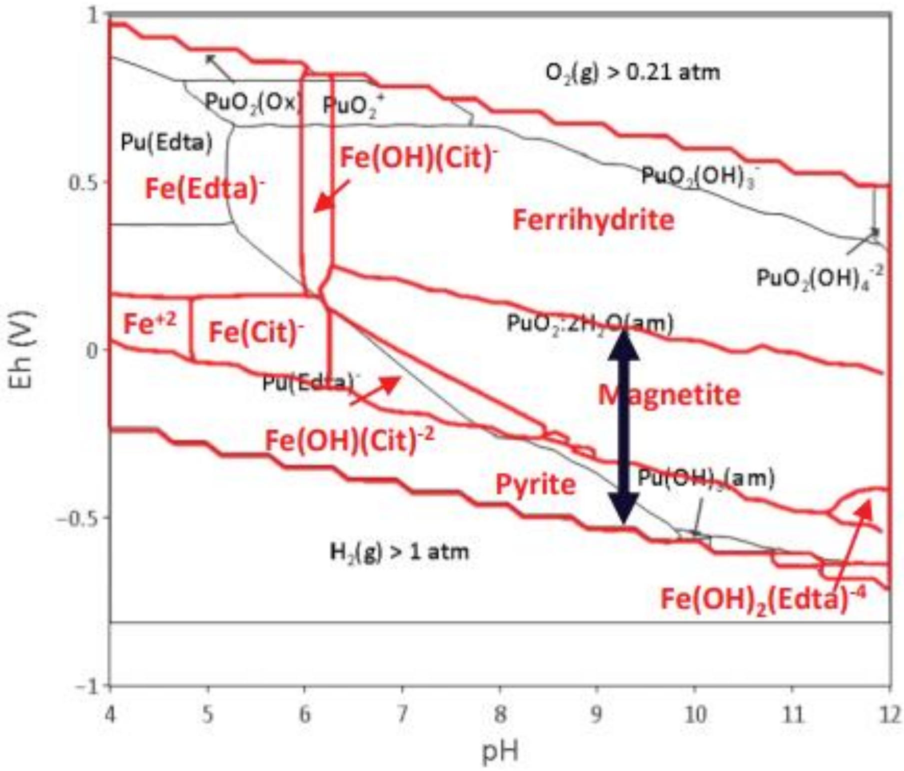

Figure 7. Pu Pourbaix diagrams in GW Brine calculated with ThermoChimie version 10a (TC10a) WIPP-2 in the presence of organic ligands, with $[Pu]_T=1 \bullet 10^{-8}$ M [Reed et al. 2020].

Another important result of this study is that while the high ionic strength in the WIPP brine solution increases the Pu solubility, it was determined that the Pu adsorbed on the corrosion products and in the solid phase, i.e., in the precipitate region, did not complex with any brine component. This also indicates that the oxidation state and speciation of Pu in the liquid phase should be investigated in more detail in future studies.

A formal summary of the expected oxidation states under WIPP conditions will be generated in a parameter update report to support the overall WIPP PA assumptions and establish them to be conservative with respect to overall Pu oxidization state distributions.

5.0 QUALITY ASSURANCE, DATA TRACEABILITY AND DOCUMENTATION

All of the data presented in this report, unless specified otherwise, were generated as Quality Level-1 data, in accordance with the CBFO QAPD. Experiments were performed under the test plan, “Effects of Radiolysis, Organic Complexation, and Redox Conditions on the Speciation and

Oxidation state distribution of Pu(III/IV)" (LCO-ACP-25). Descriptions of the experiments can be found in the scientific notebook designated ACP-25-01.

6.0 APPENDIX

6.1 UV-Vis spectra of Pu(III) and Pu(IV)

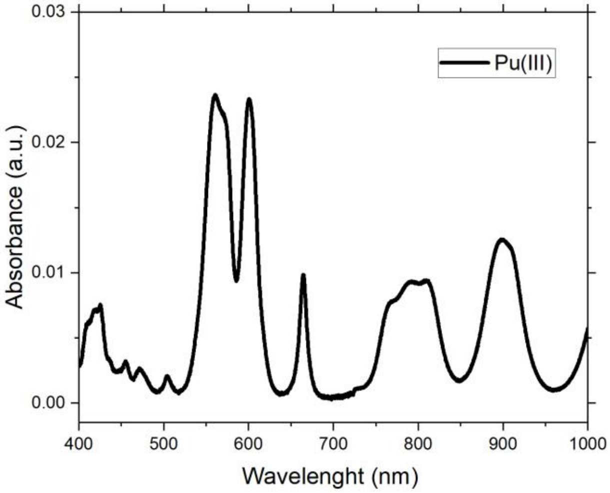

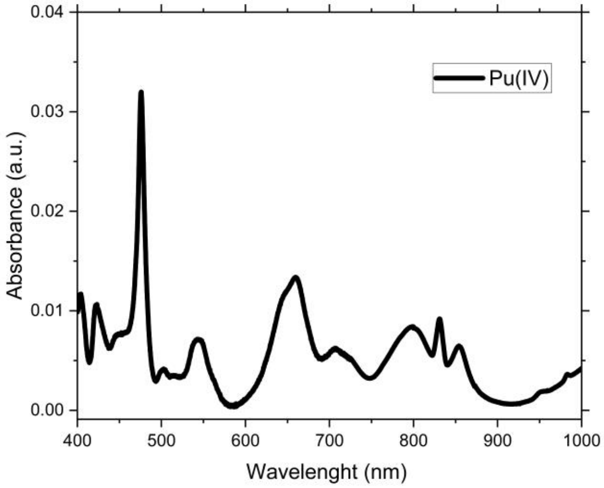

Figure 8. UV-Vis spectra of Pu (III) and Pu(IV) stock solutions.

6.2 XRD results

Iron corrosion products were analyzed both before starting the experiment and after three years of contact with synthetic WIPP brine and ^{239}Pu at $p_{C_{H+}}$ 9. After contact with Pu, the corrosion product was removed from the vials, dried and ground into powder, and to avoid cross-contamination between samples, each sample was individually wrapped in polyethylene. After three years, the

XRD measurements showed additional peaks coming from polyethylene. However, we did not observe any oxidation of magnetite and Fe^0 within the XRD detection limit (see Figures 8 and 9).

Magnetite:

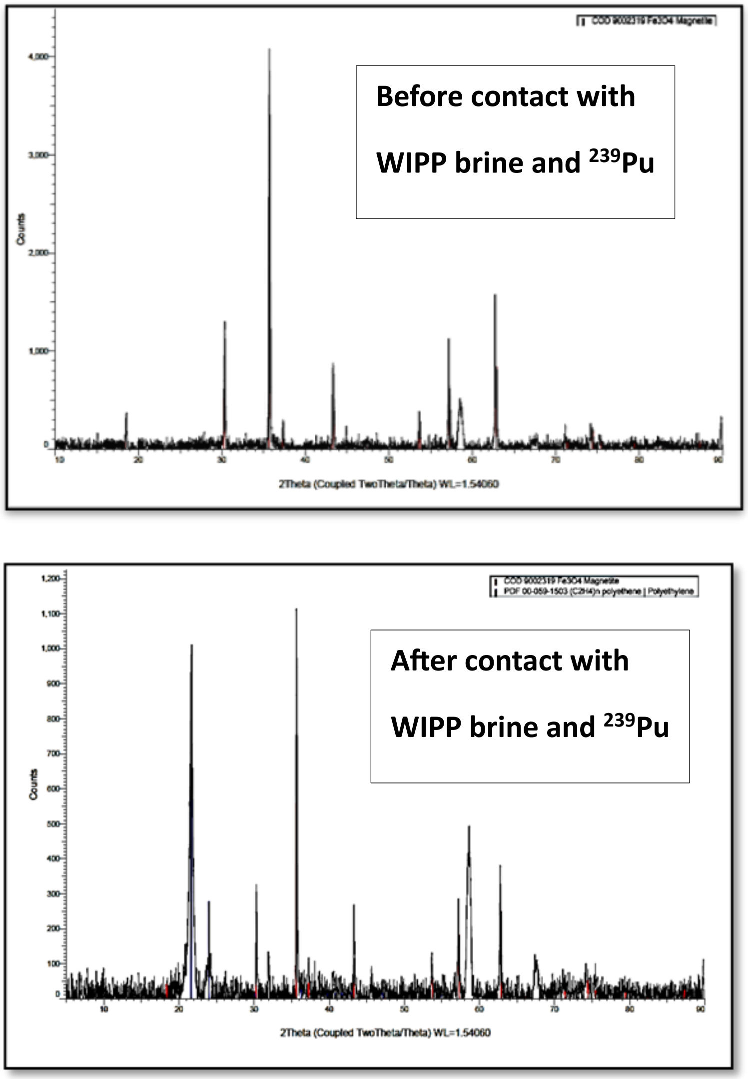

Figure 9. Room temperature XRD patterns of magnetite before and after contact WIPP brine and ^{239}Pu.

Metallic iron: Fe^0

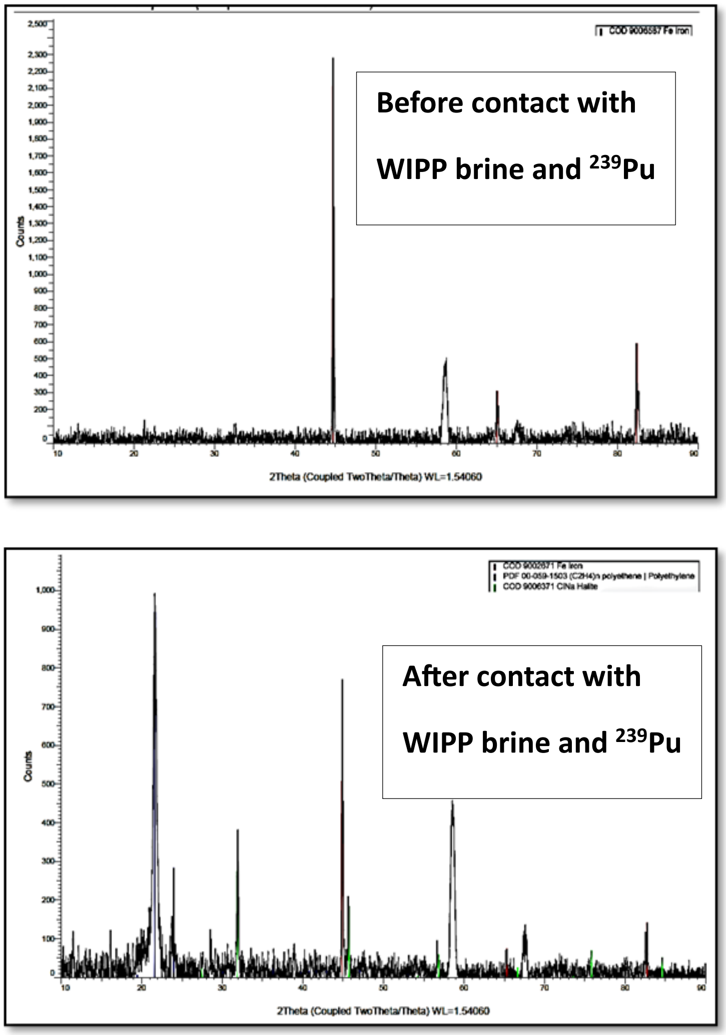

Figure 10. Room temperature XRD patterns of Fe^0 before and after contact WIPP brine and ^{239}Pu.

7.0 REFERENCES

Almahamid, I., Becraft, K. A., Hakem, N. L., Gatti, R. C., and Nitsche, H. (1996). Stability of various plutonium valence states in the presence of NTA and EDTA. Radiochimica Acta, 74, 129-134.

Altmaier, M., Metz, V., Neck, V., Müller, R., and Fanghänel, T. (2003). Solid-liquid equilibria of $Mg(OH)_2(cr)$ and $Mg_2(OH)_3Cl\cdot 4H_2O(cr)$ in the system Mg-Na-H-OH-Cl- H_2O at 25°C. Geochimica et. Cosmochimica Acta, 67(19), 3595–3601. https://doi.org/10.1016/S0016-7037(03)00165-0.

Altmaier, M., Neck, V., Ltützenkirchen, J., and Fanghänel, T. (2009). Solubility of plutonium in $MgCl_2$ and $CaCl_2$ solutions in contact with metallic iron. Radiochimica Acta, 97(4–5), 187–192. https://doi.org/10.1524/ract.2009.1593.

Altmaier, M., Gaona, X., Fellhauer, D., and Buckau, G. (2010). Intercomparison of redox determination methods on designed and near-natural aqueous systems: FP 7 EURATOM Collaborative Project "Redox Phenomena Controlling Systems" (KIT Scientific Reports; 7572).

Altmaier, M., Gaona X., Fanghänel, T. (2013). Recent advances in aqueous actinide chemistry and thermodynamics. Chemical Reviews 113 (2), 901-943. DOI: 10.1021/cr300379w.

Ankudinov, A. L., Bouldin, C. E., Rehr, J. J., Sims, J., and Hung, H. (2002). Parallel calculation of electron multiple scattering using Lanczos algorithms. Physical Review B - Condensed Matter and Materials Physics, 65(10), 1041071–10410711. https://doi.org/10.1103/PhysRevB.65.104107.

Asami, K., and Kikuchi, M. (2003). In-depth distribution of rusts on a plain carbon steel and weathering steels exposed to coastal-industrial atmosphere for 17 years. Corrosion Science, 45(11), 2671–2688. https://doi.org/10.1016/S0010-938X(03)00070-2.

Ashley, G. W. and Burstein, G. T. (1991). Initial stages of the anodic oxidation of iron in chloride solutions. Corrosion 47, 908-916.

Balboni, E., Smith, K. F., Moreau, L. M., Li, T. T., Maloubier, M., Booth, C. H., Kersting, A. B., and Zavarin, M. (2020). Transformation of ferrihydrite to goethite and the fate of plutonium. ACS Earth and Space Chemistry, 4(11), 1993–2006.

Belin, R. C., Valenza, P. J., Reynayd, M. A., and Raison, P. E. (2004). New hermetic sample holder for radioactive materials fitting to Siemens D5000 and Bruker D8 x-ray diffractometers: application to the rietveld analysis of plutonium dioxide. Journal of Applied Crystallography, 37(6), 1034–1037. https://doi.org/10.1107/S0021889804022885.

Borkowski, M., Lucchini, J.-F., Richmann, M. K., and Reed, D. T. (2009). Actinide (III) solubility in WIPP brine: data summary and recommendations. https://api.semanticscholar.org/CorpusID:92450688.

Cho, W. J., Kwon, S., and Park, J. H. (2008). KURT, a small-scale underground research laboratory for the research on a high-level waste disposal. Annals of Nuclear Energy, 35(1), 132–140. https://doi.org/10.1016/j.anucene.2007.05.011.

Chtoun, E., Hanebali, L., Garnier, P., and Kiat, J. M. (1997). X-rays and neutrons rietveld analysis of the solid solutions (1-x)($A_2Ti_2O_7$) - x($MgTiO_3$) (A = Y or Eu). European Journal of Solid State and Inorganic Chemistry 34, p. 553-561.

Clark, D. L. (2000). The chemical complexities of plutonium. Los Alamos Science 26, 392–411.

Cobas, J. E., and Søgaard, E. G. (2022). Chelating agents for diluted geothermal brine reinjection. Geothermal Energy, 10(1). https://doi.org/10.1186/s40517-022-00227-1.

Comins, M. B., Kaplan, U., Beam, J., Navarrette, A., and Hixon, A. E. (2024). Plutonium speciation and oxidation state distributions in the presence of citrate. Environmental Science and Technology, 58(35), 15766–15778. https://doi.org/10.1021/acs.est.4c02803.

Cook, D. C. (2005). Spectroscopic identification of protective and non-protective corrosion coatings on steel structures in marine environments. Corrosion Science, 47(10), 2550–2570. https://doi.org/10.1016/j.corsci.2004.10.018.

U.S. Congress. (1996). Public Law 102-579. Waste Isolation Pilot Plant Land Withdrawal Act of 1992, as amended by Public Law 104-201. Retrieved from https://wipp.energy.gov/library/CRA/CRA%202019/T%20%20W/USC%20%201996%20%20LWA%20Public%20Law%20102-579.pdf.

Dardenne, K., Seibert, A., Denecke, M. A. and Marquardt, C. M. (2009). "Plutonium(III,IV,VI) speciation in gorleben groundwater using XAFS." Radiochimica Acta, vol. 97(2), 91-97. https://doi.org/10.1524/ract.2009.1581.

DiBlasi, N. A., Yalçintas, E., Stanley, F. E., Reed, D. T., and Hixon, A. E. (2021). Influence of ethylenediaminetetraacetic acid on the long-term oxidation state distribution of plutonium. Chemosphere, 274. https://doi.org/10.1016/j.chemosphere.2021.12974.

DiBlasi, N. A., Tasi, A. G., Trumm, M., Schnurr, A., Gaona, X., Fellhauer, D., Dardenne, K., Rothe, J., Reed, D. T., Hixon, A. E., and Altmaier, M. (2022). Pu(III) and Cm(III) in the presence of EDTA: aqueous speciation, redox behavior, and the impact of Ca(II). RSC Advances, 12(15), 9478–9493. https://doi.org/10.1039/d1ra09010k.

U.S. Department of Energy. (2023). Final Environmental Impact Statement for the Surplus Plutonium Disposition Program, DOE/EIS- 0549; U.S. Department of Energy.

Dumas, T., Fellhauer, D., Schild, D., Gaona, X., Altmaier, M., and Scheinost, A. C. (2019). Plutonium retention mechanisms by magnetite under anoxic conditions: Entrapment versus sorption. ACS Earth and Space Chemistry, 3(10), 2197–2206. https://doi.org/10.1021/acsearthspacechem.9b00147.

Duro, L., Domènech, C., Grivé, M., Roman-Ross, G., Bruno, J., and Källström, K. (2014). Assessment of the evolution of the redox conditions in a low and intermediate level nuclear waste repository (SFR1, Sweden). Applied Geochemistry 49, 192–205. https://doi.org/10.1016/j.apgeochem.2014.04.015.

Felmy, A. R., Rai, D., Schramke, J. A., and Ryan, J. L. (1989). The solubility of plutonium hydroxide in dilute solution and in high-ionic-strength chloride brines. Radiochimica Acta, 48(1-2), 29-36.

Francis, A. J., Dodge, C. J., and Gillow, J. B. (2006). Biotransformation of plutonium complexed with citric acid. Radiochimica Acta, 94, 731–737. https://doi.org/10.1524/ract.2006.94.9.731.

Geckeis, H., B. Salbu, T. Schafer, and Zavarin, M. (2016). Environmental Chemistry of Plutonium. LLNL-BOOK-688957.

Gerle, M. (2022). Annual Transuranic Waste Inventory Report, DOE/TRU-22-3425; U.S. Department of Energy, Carlsbad Field Office.

Glazyrin, K., McCammon, C., Dubrovinsky, L., Merlini, M., Schollenbruch, K., Woodland, A. and Hanfland, M. (2012). Effect of high pressure on the crystal structure and electronic properties of magnetite below 25 GPaAmerican Mineralogist, 97(1), 128-133. https://doi.org/10.2138/am.2011.3862.

Honty, M., and de Craen, M. (2009). EXTERNAL REPORT SCK•CEN-ER-87 Mineralogy of the Boom Clay in the Essen-1 borehole. SCK•CEN-ER-87, 09/MHo/P-35.

Hoth, P., Wirth, H., Reinhold, K., Bräuer, V., Krull, P., Feldrappe, H., and Berlin, T. (2007). Endlagerung radioaktiver Abfälle in tiefen geologischen Formationen Deutschlands-Untersuchung und Bewertung von Tongesteinsformationen. BGR, Berlin/Hannover, April 2007.

Hu, Y., Kestrel Schwaiger, L., Booth, C. H., Kukkadapu, R. K., Cristiano, E., Kaplan, D., and Nitsche, H. (2010). Molecular interactions of Plutonium(VI) with synthetic manganese-substituted goethite. Radiochimica Acta, vol. 98(9-11), 655-663. https://doi.org/10.1524/ract.2010.1766.

Kaul, A., and Roethemeyer, H. (1997). Investigation and evaluation of the Gorleben site: a status report. In Nuclear Engineering and Design. Volume 176, Issues 1–2, Pages 83-88 https://doi.org/10.1016/S0029-5493(96)01345-3.

Kosakowski, G., and Scherrer, P. (2004). Time-dependent Flow and Transport Calculations for Project Opalinus Clay (Entsorgungsnachweis), NAGRA NTB 03-10.

Lemire, R. J. (2001). Chemical thermodynamics of neptunium and plutonium. https://api.semanticscholar.org/CorpusID:92957809.

Li, W., Liang, X., An, P., Feng, X., Tan, W., Qiu, G., Yin, H., and Liu, F. (2016). Mechanisms on the morphology variation of hematite crystals by Al substitution: The modification of Fe and O reticular densities. Scientific Reports, 6, 35960. https://doi.org/10.1038/srep35960.

MacFarlane, D.R. and S.I. Smedley. (1986). The dissolution mechanism of iron in chloride solutions. Journal of the. Electrochemical Society 133, 2240-2244.

Martin, P., Grandjean, S., Valot, C., Carlot, G., Ripert, M., Blanc, P., and Hennig, C. (2007). XAS study of $(U_{1-y}Pu_y)O_2$ solid solutions. Journal of Alloys and Compounds, 444–445 (SPEC. ISS.), 410–414. https://doi.org/10.1016/j.jallcom.2007.01.032.

McFadden, K. M. (1980). Organic components of nuclear wastes and their potential for altering radionuclide distribution when released to soil. (No. PNL-2563). Battelle Pacific Northwest Labs., Washington, DC.

Micheau, C., Virot, M., Dourdain, S., Dumas, T., Menut, D., Solari, P. L., Venault, L., Diat, O., Moisy, P., and Nikitenko, S. I. (2020). Relevance of formation conditions to the size, morphology and local structure of intrinsic plutonium colloids. Environmental Science: Nano, 7(8), 2252–2266. https://doi.org/10.1039/d0en00457j.

Neck, V., Altmaier, M., and Fanghänel, T. (2007). Solubility of plutonium hydroxides/hydrous oxides under reducing conditions and in the presence of oxygen. Comptes Rendus Chimie, 10(10–11), 959–977. https://doi.org/10.1016/j.crci.2007.02.011.

Nemer, M. B., Xiong Y., Ismail, A. E., Jang, J. (2011). Solubility of $Fe_2(OH)_3Cl$ (pure-iron end-member of hibbingite) in NaCl and Na_2SO_4 brines. Chemical Geology Volume 280, Issues 1–2, Pages 26-32. https://doi.org/10.1016/j.chemgeo.2010.10.003.

Neu, M.P., Goff, G.S. and Runde, W. (2011). Plutonium: Radionuclides. In Encyclopedia of Inorganic and Bioinorganic Chemistry, R.A. Scott (Ed.). https://doi.org/10.1002/9781119951438.eibc0437.

Newville, M. (2013). Larch: An analysis package for XAFS and related spectroscopies. Journal of Physics: Conference Series, 430(1). https://doi.org/10.1088/1742-6596/430/1/012007.

Safety of geological disposal of high-level and long-lived radioactive waste in France: an international peer review of the “Dossier 2005 Argile” concerning disposal in the Callovo-Oxfordian formation. (2006). Nuclear Energy Agency, OECD.

Rai, D., Bolton, H., Moore, D. A., Hess, N. J., and Choppin, G. R. (2001). Thermodynamic model for the solubility of PuO_2(am) in the aqueous Na^+-H^+-OH^--Cl^--H_2O-ethylenediaminetetraacetate system. Radiochimica. Acta 89(36923), 67-74.

Rai, D., Moore, D. A., Rosso, K. M., Felmy, A. R., and Bolton, H. (2008). Environmental mobility of Pu(IV) in the presence of ethylenediaminetetraacetic acid: myth or reality? Journal of Solution Chemistry, 37(7), 957–986. https://doi.org/10.1007/s10953-008-9282-2.

Reich, T., Geipel, G., Funke, H., Hennig, C., Roßberg, A., and Bernhard, G. (2001). XANES and EXAFS measurements of plutonium hydrates. In Biannual Report 1999/2000, FZR-322; Project-Group ESRF-Beamline (ROBL-CRG), 2001; pp 27–32.

Reich, T., Reich, T. Ye., Amayri, S., Drebert, J., Banik, N. L., Buda, R. A., Kratz, J. V., and Trautmann, N. (2007). Application of XAFS spectroscopy to actinide environmental science. AIP Conference Proceedings, 882, 179–183. https://doi.org/10.1063/1.2644467.

Reed, D. T., Coli, E., Garcia, D., and Duro, L. (2020). Systematic Calculation of Pu Pourbaix Diagrams: Modelling Support for the LANL ACRSP Team. United States. doi:10.2172/1734695. Runde, W., (2000). Chemical Interactions of Actinides in the Environment. Number 26, Los Alamos Science

Schmeide, K., Reich, T., Sachs, S., and Bernhard, G. (2006). Plutonium(III) complexation by humic substances studied by X-ray absorption fine structure spectroscopy. Inorganica Chimica Acta, 359(1), 237–242. https://doi.org/10.1016/j.ica.2005.10.037.

Schramke, J. A., Santillan, E. F. U., and Peake, R. T. (2020). Plutonium oxidation states in the Waste Isolation Pilot Plant repository. Applied Geochemistry, 116. https://doi.org/10.1016/j.apgeochem.2020.104561.

Serne, R. J., Cantrell, K. J., Lindenmeier, C. W., Owen, A. T., Kutnyakov, I. V., Orr, R. D., and Felmy, A. R. (2002). Radionuclide-chelating agent complexes in low-level radioactive decontamination waste; stability, adsorption and transport potential. U.S. Nuclear Regulatory Commission NUREG/CR-6758, PNNlL13774.

Smith, K. F., Morris, K., Law, G. T. W., Winstanley, E. H., Livens, F. R., Weatherill, J. S., Abrahamsen-Mills, L. G., Bryan, N. D., Mosselmans, J. F. W., Cibin, G., Parry, S., Blackham, R., Law, K. A., and Shaw, S. (2019). Plutonium(IV) sorption during ferrihydrite nanoparticle formation. ACS Earth and Space Chemistry, 3(11), 2437–2442. https://doi.org/10.1021/acsearthspacechem.9b00105.

Stagg, O., Morris, K., Townsend, L. T., Kvashnina, K. O., Baker, M. L., Dempsey, R. L., Abrahamsen-Mills, L., and Shaw, S. (2022). Sulfidation and reoxidation of U(VI)-incorporated goethite: implications for U retention during sub-surface redox cycling. Environmental Science and Technology, 56(24), 17643–17652. https://doi.org/10.1021/acs.est.2c05314.

Tasi, A., Gaona, X., Fellhauer, D., Böttle, M., Rothe, J., Dardenne, K., Schild, D., Grivé, M., Colàs, E., Bruno, J., Källström, K., Altmaier, M., and Geckeis, H. (2018). Redox behavior and solubility of plutonium under alkaline, reducing conditions. Radiochimica Acta, 106(4), 259–279. https://doi.org/10.1515/ract-2017-2870.

Thakur, P., Pathak, P. N., and Choppin, G. R. (2009). Complexation thermodynamics and the formation of the binary and the ternary complexes of tetravalent plutonium with carboxylate and amino carboxylate ligands in aqueous solution of high ionic strength. Inorganica Chimica Acta, 362(1), 179–184. https://doi.org/10.1016/j.ica.2008.03.127.

Tosca, N. J., Ahmed, I. A. M., Tutolo, B. M., Ashpitel, A. and Hurowitz, J. A. (2018). Magnetite authigenesis and the warming of early mars. Nature Geoscience, 11(9), 635-639. DOI: 10.1038/s41561-018-0203-8.

Toste, A. P. (1992). Degradation of chelating and complexing agents in an irradiated, simulated mixed waste. Journal of Radioanalytical and Nuclear Chemistry, 16(2), 549-559.
Toste, A. P., and Lechner-Fish, T. J. (1993). Chemo-degradation of chelating and complexing agents in a simulated, mixed nuclear waste. Waste Management 13(3), 237-244.

U.S. Department of Energy. (2023). Quality Assurance Program Document (QAPD), DOE/CBFO-94-1012, Rev. 14. Carlsbad Field Office. Carlsbad NM.

Van Soest, G. D. (2018). Performance assessment inventory report 2018. Carlsbad NM.

Wang, Z., Moore, R. C., Felmy, A. R., Mason, M. J. and Kukkadapu, R. K., (2000). A study of the corrosion products of mild steel in high ionic strength brines. Waste Management, 21(4), 335-341. https://doi.org/10.1016/S0956-053X(00)00058-1.

Wolery, T. J. (2008). Analysis Plan for EQ3/4 Analytical studies. AP-140, Rev. 0 May, 15, 2008. Carlsbad, NM. Sandia National Lab. ERMS 550239.

Xiong, Y.-L. (2011). Release of EQ3/6 database DATAA0FM1. Sandia National Lab. ERMS 555152.